Ultraclean layers and optically thin clouds in the stratocumulus to cumulus transition: part I. Observations

Robert Wood*, Kuan-Ting O, Christopher, S. Bretherton, Johannes Mohrmann

Department of Atmospheric Sciences, University of Washington, Seattle, USA

Bruce. A. Albrecht, Paquita Zuidema

Rosenthiel School of Marine and Atmospheric Sciences, University of Miami, USA

Virendra Ghate, Chris Schwartz

Argonne National Laboratory, Lemont, USA

Ed Eloranta

University of Wisconsin, Madison, USA

Susanne Glienke, Raymond Shaw

Michgan Technological University, Houghton, USA

Jacob Fugal

Max Planck Institute for Chemistry, Mainz, USA

Patrick Minnis

NASA Langley Research Center, Virginia, USA

*Corresponding author address: Robert Wood, 718 ATG Building, Department of Atmospheric Sciences, University of Washington, Seattle, WA 98112, United States of America

E-mail: robwood2@uw.edu

ABSTRACT

A common feature of the stratocumulus to cumulus transition (SCT) is the presence of layers in which the concentration of particles larger than 0.1 μm is below 10 cm^{-3}. These *ultra clean layers* (UCLs) are explored using aircraft observations from 14 flights of the NSF/NCAR G-V aircraft between California and Hawaii. UCLs are commonly located in the upper part of decoupled boundary layers, with coverage increasing from only a few percent within 500 km of the Californina coast to $\sim$30-60% west of 130°W. Most clouds in UCLs are thin, horizontally extensive layers containing drops with median volume radii ranging from 15-30 μm. Many UCL clouds do not fully attenuate the G-V lidar, and yet are frequently detected with a 94 GHz radar with a sensitivity of around -30 dBZ. Satellite data indicate that UCL clouds have visible reflectances of $\sim$0.1-0.2 and are often quasi-laminar, giving them a veil-like appearance. These veil clouds exist for 1-3 hours or more, are associated with mesoscale cumulus clusters, and likely grow by spreading under strong inversions. Active updrafts in the Cu clouds have droplet concentrations of $\sim$25-50 cm^{-3}. Collision-coalescence in the Cu, and later sedimentation in the thinner UCL clouds, are likely the key processes removing droplets in UCL clouds. UCLs are relatively quiescent, and a lack of mixing with dry air above and below the cloud may help to explain their longevity. The very low and highly variable droplet concentrations in UCL clouds, together with their low geometrical thickness, makes these clouds particularly challenging to represent in large scale models.

1. Introduction

Assessment of the physical factors controlling the coverage and albedo of marine boundary layer (MBL) clouds remains a pressing challenge. The speed at which the stratocumulus (Sc) to Cumulus (Cu) transition (SCT) occurs in air masses downstream of the eastern subtropical ocean basins determines the albedo of the Tropics, and similar cloud transitions in post-frontal air masses are important for determining midlatitude storm track albedo. These transitions in cloudiness are poorly represented in climate models, which typically show stratocumulus break-up occurring too quickly in both the subtropics (Teixeira et al., 2011) and the midlatitudes (Williams et al., 2012; Bodas-Salcedo et al., 2014). In addition to producing too few low clouds, model clouds are too reflective, a pathology commonly referred to as the "too-few, too-bright" problem (Nam et al., 2012; Engstrm et al., 2015).

In general, the SCT initiates in response to MBL deepening and decoupling as surface fluxes increase over warmer waters (Bretherton and Wyant, 1997; Wyant et al., 1997). As several studies have shown (Martin et al., 1995; Zhou et al., 2015), stratocumulus cloud breakup is not an immediate response to MBL decoupling, but can be delayed by as much as 1-3 days, with cloud cover often remaining above 50% until 500-2000 km downsteam of decoupling onset (Zhou et al., 2015). Given the importance of the SCT, it is remarkable that few dedicated aircraft observations have sampled the MBL in the breakup region owing to the typically remote location of this phenomenon and the limited range of most research aircraft. Early transition experiments with shipborne observations (e.g., the 1969 Airmass Transition Experiment, ATEX, Augstein et al., 1973; Stevens et al., 2001) provided important characterization of the vertical thermodynamic structure of the MBL under transition conditions, but little if any information on cloud structure and dynamics. Aircraft observations made during the Atlantic Stratocumulus Transition Experiment (ASTEX) in 1992

provide one of the most widely used datasets for understanding the SCT and are perhaps the first measurements of cloud microphysical properties in the SCT. The two Lagrangian transition experiments carried out in ASTEX showed that drizzle occurred with sufficient frequency and rate to be important in MBL energy and moisture budgets (Bretherton and Pincus, 1995; Bretherton et al., 1995). Surface-based radar measurements in ASTEX also hightlighted the frequent occurrence of precipitating cumulus clusters with horizontal scales of $\sim$10 km rising into and interacting with stratocumulus clouds at the top of the decoupled MBL (Miller and Albrecht, 1995). Martin et al. (1995) showed that the stratocumulus deck is locally thickened in regions of interaction with rising Cu, consistent with the Cu providing a source of moisture to the decoupled cloud layer aloft. However, the Cu also drive entrainment of dry air from the free troposphere, which eventually serves to dry the upper MBL and dissipate the Sc (Krueger et al., 1995; Wyant et al., 1997). The timescale over which drying happens, i.e., the time between decoupling and stratocumulus break up, likely depends upon the relative amount of free tropospheric entrainment that is achieved for a given Cu mass flux, the inversion strength (which influences both entrainment and the spreading of Cu below the inversion), the free-tropospheric humidity, and the rate at which the upper MBL loses condensate through precipitation and droplet sedimentation. The processes causing drying therefore are expected to depend upon the nature of the clouds and turbulent dynamics in the upper MBL.

Large eddy simulations (LES) indicate that the SCT is sensitive to cloud microphysical processes in addition to large scale meteorological controls. Sandu and Stevens (2011) found that reducing the cloud droplet concentration N_d (assumed to be constant throughout the domain and over the simulation time) from 100 to 33 cm^{-3} increases precipitation efficiency and slows down the growth of the MBL, but hastens the rate of cloudiness reduction. Although not specifically transition experiments, previous short-duration LES studies have shown a strong dependence of

stratocumulus cloud cover on N_d (Ackerman, 2003), especially when N_d falls below 50 cm^{-3}. This result is broadly consistent with the Sandu and Stevens (2011) study, pointing to the need to understand what controls N_d in the SCT.

Several cases of spatial transitions from closed to open cellular convection over the southeastern Pacific Ocean were observed during the VOCALS Regional Experiment (Terai et al., 2014), and showed that within regions of open cells, active Cu clouds that draw aerosol from the surface mixed layer have N_d values approximately three times larger than the layer of thin stratus/stratocumulus at the top of the MBL into which the Cu are detraining. Further, N_d in the stratus layer of the open cell region was found to be extremely low (5 cm^{-3} in the mean, over five cases), prompting its characterization as an *ultra clean layer* (UCL), a term first used for clean, thin unpolluted layers between aerosol-rich polluted layers over southern Africa (Hobbs, 2003). In one open cell case during VOCALS, N_d in the most active Cu updrafts was over an order of magnitude greater than that in the relatively quiescent detrained stratus layer (Wood et al., 2011). Other observational studies have found cases with extremely low N_d and cloud condensation nuclei concentrations in the subtropical MBL (Stevens et al., 2005; Sharon et al., 2006; Petters et al., 2006; Wood et al., 2008), in midlatitude marine cold air outbreaks (Field et al., 2014) and in the Arctic (Mauritsen et al., 2011). Combining data from satellite with ship cruises between California and Hawaii, Painemal et al. (2015) showed using that the correlation of satellite N_d and surface-based accumulation aerosol concentration was 0.9 east of 145°W, but dropped to 0.5 in the SCT west of this, consistent with a decoupling of cloud microphysics from near-surface aerosol and surface aerosol sources in the SCT. This would be consistent with an aerosol sink in the upper PBL that is uncorrelated with near-surface aerosol.

The dramatic variability of N_d even within the same cloud system raises the question of whether fixing N_d (or aerosol concentration) across an entire model domain is appropriate for the study of

the SCT. Recent LES studies (e.g., Kazil et al., 2011; Berner et al., 2013) have allowed N_d and aerosols to vary spatiotemporally in response to coalescence scavenging and Brownian scavenging, surface particle fluxes, entrainment, and advection. These studies have been able to repoduce with some fidelity the vertical and horizontal variability of N_d and aerosol concentration in the MBL seen in the open cell cases observed in VOCALS. A dramatic reduction in N_d due primarily by coalescence scavenging appears to be a universal feature of the transition from closed to open cells, although the level of sophistication in the aerosol budget necessary to faithfully reproduce the cloudiness transition is unclear. What is also unclear is the extent to which closed to open cell transitions and specifically the formation of UCLs are representative of the behavior of SCTs observed elsewhere.

This study explores the nature of clouds and aerosols in the upper MBL occurring in the SCT, with specific focus on understanding the relationship between ultra-clean layers (UCLs) and frequently-occurring optically thin clouds in these layers. The primary tool is aircraft observations from fourteen flights of the NSF/NCAR G-V aircraft during the Cloud System Evolution in the Trades (CSET) field program. CSET sampled the MBL and lower free troposphere extending across the entire region from the Californian coast ($\sim$38°N, 123°W) to Kona, Hawaii (19°N, 156°W), a distance of 3700 km. Trajectory calculations indicate that air-masses take approximately five days to advect this distance (Sandu et al., 2010), offering unprecedented observations of the complete transition from shallow marine stratocumulus and stratus, to deep well-mixed and then decoupled Sc, through to a largely trade Cu environment at Hawaii, albeit one with 40% coverage by optically thin upper PBL stratiform clouds. Section 2 describes the observational datasets used and the methodological approach. Section 3 examines the statistical occurrence of both clear and cloudy UCLs including their frequency, altitude, and geographical distribution. Section 4 documents properties of both cloudy and clear UCLs using *in situ* G-V data. Section 5

explores several case studies from CSET, combining *in situ* and remote sensing data from the G-V in conjunction with satellite remote sensing, to provide further insights into the microphysical and macrophysical structure of UCLs and optically thin clouds. Section 6 documents the statistical properties of optically thin MBL clouds observed in CSET, relating their vertical structure to that of cloudy UCLs. Finally, Section 7 introduces hypotheses for how UCLs are formed and discusses some of the implications of the results presented in this study.

2. Data and methods

a. Instruments and sampling

Data from the Cloud System Evolution in the Trades (CSET) field campaign (Albrecht, 2017) constitute the primary observational dataset used in this study. The NSF/NCAR Gulfstream-V High-performance Instrumented Airborne Platform for Environmental Research (G-V HIAPER) aircraft sampled marine air masses between Sacramento, California (38.6°N, 121.5°W) and Kona, Hawaii (19.6°N, 156.0°W). The G-V was instrumented with numerous instruments, which are detailed in Albrecht (2017) and are only described briefly here. In addition to measurements of the atmospheric state variables (temperature, pressure, water vapor, and winds including high frequency turbulent components at 20 Hz), other instruments used in this study include:

- an Ultra High Sensitivity Aerosol Spectrometer (UHSAS) that measures aerosol particles with diameters from 60-1000 nm, with 100 size bins. Here, we use only the most reliable size bins from 100-1000 nm and define N_a as the concentration of particles larger than 100 nm. UHSAS data are used only in cloud-free conditions;

- Cloud droplet probe, measuring the cloud droplet size distribution from 1-25 μm radius (with a 1 μm bin width), and a fast 2D-C optical array probe to provide a size distribution for larger

drops between 37.5 and 800 μm radius with a bin width of 12.5 μm radius. The concentration of drops measured by the CDP is termed the droplet concentration N_d. The CDP and 2D-C data are combined to produce a single cloud-drizzle size distribution from 1-800 μm, with spline interpolation in log-log space used to fill the gap region between the upper size bin of the CDP and the smallest useable bin of the 2D-C; in addition to the CDP and 2D-C probes, the G-V also flew a holographic cloud droplet detector (HOLODEC) (Fugal and Shaw, 2009) that uses holographic reconstruction to measure droplets spanning the poorly measured gap region.

- King hotwire probe to measure liquid water content;

- A VCSEL water vapor hygrometer and a Rosemount temperature sensor;

- HIAPER Cloud Radar (HCR), a 94 GHz Doppler radar that can sample either in the nadir or zenith directions (Vivekanandan et al., 2015). Nadir sampling is used when the aircraft is above cloud or in cloud layers, and zenith sampling is used when the aircraft is below the cloud level;

- High Spectral Resolution Lidar (HSRL), a 532 nm lidar (Grund and Eloranta, 1991) that can sample either in near-nadir or near-zenith directions. The lidar is manually turned from nadir to zenith sampling and the pointing direction is set to be almost the same as that for the HCR, except that the HSRL is designed to be pointed 4° laterally off-nadir/zenith to avoid specular reflections from ice crystals.

We use all available data from fourteen of the research flights (RF02 through RF15) that were designed to sample airmasses transitioning from Sc to Cu. The outbound flights (Sacramento to Kona) comprised a transit leg (typically at 6-8 km altitude) from Sacramento to an offshore

location containing Sc clouds relatively close to the Californian coast. The G-V then profiled down to conduct low-level sampling of the PBL and lower free troposphere (FT) for a horizontal distance of typically 1500-2000 km before ascending again to ∼6 km for the transit to Kona. Low-level sampling constituted approximately half of the flight. The return flight from Kona to Sacramento was conducted two days after the outbound flight and was designed to sample the locations of the Lagrangian-advected PBL airmasses that had moved toward Hawaii over the two days between the outbound and return flights. The return flight consisted of approximately the same amount of low level sampling as was carried out on the outbound flight. The locations of the flights are shown in (Albrecht, 2017). The low-level sampling strategy consisted of repeated flight modules comprising a 10 min near-surface straight and level leg (∼140 m above the surface), a 10 min straight and level leg 100 m above the cloud base (either the Sc cloud base for overcast conditions or the Cu cloud base for broken cloud conditions), a sawtooth leg porpoising from approximately 100 m below cloud top to 400 m above cloud top (with three upward inversion crossings and two downward), a 10 min straight and level leg in the FT approximately 1000 m above cloud top, and then a profile from this level down to the near-surface (140 m altitude). This sampling strategy was designed to provide somewhat representative horizontal and vertical *in situ* sampling of the PBL and the lower FT, as well as good opportunities for remote sensing of clouds and precipitation.

b. UCL Definition

This study focuses upon the nature and occurrence of ultra clean layers (UCLs) over the subtropical northeastern Pacific Ocean. We use G-V *in situ* cloud and aerosol properties to identify UCLs and to characterize their physical properties. Over the southeastern Pacific (Terai et al., 2014), UCLs were found in all cases of mesoscale open cellular convection, and in these cases typically

assumed the form of horizontally extensive layers in the upper PBL below the trade inversion. These layers typically consist of patches of clear air and patches of cloudy air. In cloud-free conditions, UCLs were marked by very low concentrations of accumulation mode aerosol (N_a defined in Terai et al. (2014) and here as particles with diameters larger than 0.1 μm), whereas under cloudy conditions UCLs can be identified by very low cloud droplet concentrations (N_d, droplets with radii larger than 1 μm). Defining UCLs requires the choice of thresholds, and this is somewhat arbitrary. We note that mean concentrations (N_a or N_d in the upper PBL during cases of open cells over the southeastern Pacific were generally below 10 cm^{-3} (Terai et al., 2014), which is 5-25 times lower than typical mean concentrations found in previous field studies of marine stratocumulus (see e.g., Martin et al., 1994; Miles et al., 2000). There have been very few studies that have noted such low particle concentrations, yet as we shall see these occur relatively frequently in the SCT. We therefore set a threshold for N_a or N_d of 10 cm^{-3} to distinguish UCLs from "non UCL" samples.

The procedure for classifying samples is as follows. We begin with G-V aircraft data sampled at 1 Hz, or roughly 150 m along the flight direction. This is not necessarily the native frequency of the measurements, but placing all the measurements for each flight into a single universal time frame allows the use of multiple instruments and criteria to classify air samples. We first classify each 1 Hz sample as into one of the following: (a) clear samples, (b) cloudy samples, or (c) samples containing precipitation under subsaturated conditions.

- (a) Clear samples must satisfy the following: liquid water content measured using the CDP $q_{l,CDP}$ must be lower than 0.01 g kg^{-1}, liquid water content $q_{l,2DC}$ measured using the 2D$-$C probe must be lower than 0.001 g kg^{-1}, and the total drizzle drop concentration N_{2DC} measured with the 2D-C probe must not exceed 1 liter^{-1};

- (b) Cloudy samples must have $q_{l,CDP} > 0.01$ g kg^{-1} and must have relative humidity exceeding 95%.

- (c) Samples containing precipitation under unsaturated conditions have either $q_{l,CDP} > 0.01$ g kg^{-1} or $q_{l,2DC} > 0.001$ g kg^{-1}, or $N_{2DC} > 1$ liter^{-1}, and must have relative humidity below 95%.

Following classification of samples into cloud, clear and unsaturated precipitation, each of the cloudy and clear 1 Hz samples is then classified as being either a UCL sample or a non-UCL sample using the following criterion

- (a) To be classified as a clear UCL, the 1 Hz sample must be classified as clear and further must have $N_a < 10$ cm^{-3};

- (b) To be classified as a cloudy UCL, the 1 Hz sample must be classified as cloud-containing and must have $N_d < 10$ cm^{-3}.

Once each 1 Hz sample has been classified, statistical analysis is performed as described in the next section.

3. UCL occurrence statistics

Longitude-height cross sections of UHSAS N_a from RF02 to RF15 (Fig. 1) show that very low concentrations ($<$10 cm^{-3}) commonly occur, especially west of $\sim$135°W. It is rare that these layers of very low N_a extend to the surface but instead tend to be concentrated at altitudes of 1-2.5 km, with the deeper cases mostly occurring in the western half of the region. Most flights indicate the presence of UCLs ($N_a <$10 cm^{-3}) extending some distance between California and Hawaii, but there is considerable variability between cases. For example, RF07 shows that UCLs were sampled on every leg over the $\sim$2000 km distance from 132-152°W, and were growing in

height westward with the growth in the PBL. Interestingly, RF02 and RF03, which show few UCLs, were severely impacted by biomass burning aerosol from forest fires in British Columbia that entrained into the PBL.

Using the classification described in the previous section, we analyze clear and cloudy UCLs separately. As Fig. 1 shows, the low level sampling in CSET extended from 128°W, some distance upstream of the stratocumulus maximum (climatologically at ∼135°W), to 152°W, close to Hawaii and well into the SCT breakup region. Mean low cloud cover over this longitudinal range falls from 0.7 to 0.4 (see Section 6). Our aim in this study is to examine how UCL occurrence frequency varies both with height and with longitude. To do this, we aggregate 1 Hz flight samples flight-by-flight into 5° longitude and 150 m altitude bins. The longitude bins are chosen to be sufficiently wide that they encompass an entire flight module (see section 2), providing good vertical statistics in the PBL and lower FT within a single longitude bin. Separately for clear and cloudy samples, we determine the fraction of samples in each flight/longitude/height bin that are classified as UCL samples.

An aircraft flying along a path without backtracking can only provide *in situ* measurements at a single height for any given longitude. In general, this precludes the measurement of vertically integrated quantitites such as cloud cover or UCL cover using *in situ* aircraft data. For example, the aircraft may happen to be sampling a clear region above clouds when there are clouds below. However, the rigid flight sampling strategy used in CSET, most importantly the use of predetermined flight modules along a predetermined flight track, with leg height choices objectively chosen to ensure good sampling of the PBL and lower FT, means that each flight module can provide useful information on the fraction of samples that are within UCLs. We argue that whereas the problem of estimating cloud cover with *in situ* G-V data is not well posed, an assessment of the *fraction* of clear sky and clouds that are UCLs is less biased and is statistically meaningful.

For a first look at vertical UCL statistics, we average the UCL fraction profiles over the CSET flights and longitude bins with sufficient samples to give vertical profiles of the fraction of clear and cloudy samples respectively that are diagnosed to be UCLs. To be considered sufficient, there need to be at least 20 samples in a given flight/longitude/height bin to be considered in the average. The frequency of both cloudy and clear UCLs increases with height from 0.5 km to 1.5-2 km altitude (Fig. 2). The highest fraction of clear samples classified as UCLs is approximately 20%, occurring at 1.5-1.8 km altitude. Cloudy samples are almost twice as likely to be classified as UCLs compared with clear samples, with values of 30-50% at 2 km but the vertical trends for each are quite similar. Above 2 km the clear UCL fraction falls steadily to $\sim$10% at 3 km altitude. The sampling at altitudes above 3km was too sparse to produce meaningful statistics. Below 0.5 km, there were few clouds sampled in CSET, and only 1-2% of clear samples were found to be UCLs. Above 2.0 km, there were an insufficient number of flights sampling clouds to produce statistically representative cloudy UCL fractions.

We next estimate the geographical variation of UCLs between California and Hawaii using the following approach. We seek the conditional probability (given a cloud or clear column) that the column contains a UCL *at some level*, assuming maximum vertical overlap. For each flight and 5° longitude bin with a sufficient number of samples, we identify the height bin containing the largest UCL fraction (this is done separately for cloudy and clear UCLs). Then, we average these maximum fractions over all the flights to give an estimate of the probability that a given longitude bin contains a UCL somewhere in the column. We accept that the aircraft *in situ* sampling is sparse and that this estimate of mean column UCL fraction is likely to be biased, but it is not obvious whether this will lead to a high or low bias. Assuming random overlap or maximum-random overlap rather than maximum overlap (see e.g., Morcrette and Fouquart, 1986) will lead to larger estimates of the column fraction, but we note that for many of the CSET cases, there

is a single layer (or two adjacent layers) with UCL fractions substantially higher than any of the other layers. In these cases, there is little difference between estimates assuming random and maximum overlap. On the other hand, the rather large (5° longitude) horizontal distance over which we aggregate aircraft data coupled with the limited number of samples in some height bins, may generate UCL column fraction estimates that are too high. For example, for any given flight/longitude/height bin, we only require twenty 1 Hz samples to constitute sufficient sampling. With an aircraft climb/descent rate of 500 m per minute, it takes approximately 20 seconds to profile through 150 m altitude (i.e., the thickness of our height bins). If all 20 seconds of this sampling consisted of e.g., clear UCL samples, then the clear UCL fraction would be unity and this would be carried through as the column UCL fraction for the entire longitude bin for that flight. If we increase the number of samples required before a particular bin is considered, then we exclude an increasing number of height bins from the averaging and reduce our reliability of capturing the true vertical profile.

Figure 3 shows the CSET estimated conditional probability (given cloudy or clear columns) of finding a UCL in a given column, plotted as a function of longitude along the CSET sampling region from California to Hawaii. Here, we refer to this probability as the fractional UCL coverage. UCL coverage is only few percent east of 130°W consistent with most prior observations in the region within about 500 km of the California coast where very low concentrations of aerosol and/or cloud droplets are relatively rare. A caveat is that only three of the CSET flights in this region had sufficient sampling to contribute to this average, and so our statistics are rather poor in this region. And whereas there have been some notable studies of very low aerosol and/or cloud droplet concentration clouds in the region east of 130°W (e.g., Hindman et al., 1994; Petters et al., 2006), a survey of the published literature of studies in the near-coastal Californian stratocumulus deck (see e.g., Hudson and Xie, 1999; Miles et al., 2000; Lu et al., 2007) show that very low

CCN conditions are relatively rare. This is consistent with a strong offshore gradient in cloud droplet concentration measured as seen from satellites, where near-coastal mean values exceed 100 cm^{-3} (Wood et al., 2012). West of 130°W, both clear and cloudy the UCL frequencies rise rapidly (Fig. 3) to values in the range of 40-50% between 130-140°W, and reach as high as 60% by 150°W. The westward increase for clear UCLs is somewhat less noisy than for cloudy UCLs, which also occur somewhat less frequently than clear UCLs west of 140°W. This is because the overall frequency of clouds decreases westward as the extensive stratocumulus clouds break up (thus making statistics less reliable), but may also reflect a general tendency for clear UCLs to be more horizontally extensive than cloudy UCLs. Thus even as the probability of finding a UCL cloud in any given cloudy sample is higher than it is for the clear counterparts (Fig. 2), clear UCLs tend to occur somewhere in the column more frequently than cloudy UCLs.

4. In situ properties of UCLs

a. Aerosol and cloud properties

In this section, we use the G-V *in situ* data to examine vertically-resolved characteristics of cloudy and clear UCLs. In clear UCLs, concentrations of aerosol particles with diameters exceeding 0.1 μm (N_a) decrease with height from values only slightly smaller than the threshold used to define UCLs (10 cm^{-3}) in the surface mixed layer below $\sim$600 m to values of 2-5 cm^{-3} in the height range (1-2 km) where most UCLs occur (Fig. 4(a)). Remarkably, mean cloud droplet concentrations N_d shows very similar vertical behavior up to 2 km altitude. The strong connection between the vertical profiles of N_a and N_d is consistent with the hypothesis that clear UCLs essentially result from the evaporation of UCL clouds, which being few in number results in a very low return of cloud-forming aerosol particles to the clear sky. An alternative hypothesis could be that

some UCL clouds initially form upon saturation of clear UCLs and the associated activation of a very low concentration of accumulation mode aerosol. In either case, the question of what drives the very low concentrations in the first place must be addressed.

Although accumulation mode aerosol concentrations are, by definition, very low in UCLs, the median concentration N_{CN} of condensation nuclei (particles with diameters larger than 10 nm) in clear UCLs is 50-90 cm^{-3} (Fig. 4(b)), i.e., over an order of magnitude higher than N_a. Further, median N_{CN} in clear UCLs is relatively independent of UCL altitude from the surface up to 2 km. In contrast, median N_{CN} for all clear samples exceeds 130 cm^{-3} at all levels, increasing to approximately 200 cm^{-3} in the lower free troposphere. Clear UCLs have anomalously high mean relative humidity exceeding 80% at all levels and closer to 90% in the most common UCL height range of 1-2 km (Fig. 4(b)). Clear UCLs at altitudes above 2 km show higher mean CN concentrations and lower mean RH than those layers below this, and some of these UCLs are actually in the free troposphere (FT). Probability distribution functions for clear samples below 3 km altitude (Fig. 5) show that 60% of UCLs have RH exceeding 85%. In contrast, only 28% of all clear samples have such high RH. This figure also demonstrates that roughly a quarter of clear UCLs sampled in CSET had RH lower than 50%. Since PBL RH rarely falls below 60%, such layers are UCLs in the lower FT. Therefore, UCLs are not solely a PBL phenomenon, although their frequency of occurrence in the lower FT appears to be lower than at the top of the PBL (Fig. 2).

The frequency of occurrence of UCLs occurring higher up in the FT is estimated from the CSET transit legs (altitude 6.5-7 km) that were conducted before and after the low-level sampling. Accounting for the lower density at the transit level to estimate the concentration that these layers would have when compressed adiabatically to 1.5 km altitude, we estimate UCL frequency when subsided to be approximately 15%, which is quite close to the observed frequency of clear UCLs in the lower FT (2-3 km altitude) shown in Fig. 2. Thus, it seems reasonable to conclude that

the subsiding FT has the potential to be a contributor to occurrences of UCLs found in the PBL. However, the fraction of cloudy samples classified as UCLs is much higher (30-40%) in the upper PBL (Fig. 2). Given this and the tendency for clear UCLs below 3km altitude to be associated with high RH, it seems likely that many clear UCLs in the PBL originate from the evaporation of UCL clouds in the PBL. In part II of this paper, we use a microphysical model to explore a mechanism for the production of UCL clouds, and conclude that collision-coalescence in cumulus updrafts is likely sufficient to explain the observed UCLs in the PBL.

Mean liquid water contents in UCL clouds tend to be relatively low compared with typical marine stratocumulus clouds, and the majority of the condensate tends to consist of droplets with radii exceeding 37.5 μm that are measured by the 2DC probe (Fig. 4(c)). The total condensate (approximately represented by the sum of the CDP and 2DC q_L) does not have strong height dependence and is typically 0.1-0.15 g m^{-3}. We use the CDP and 2DC size distributions to estimate the mean effective radii (r_e) of UCL clouds and find mean values of 20-25 μm (Fig. 4(d)). As might be expected given that droplets in the 2DC size range constitute the majority of the condensate, the mean effective radii derived from only the CDP probe (droplets with radii smaller than 25 μm) are considerably smaller (see e.g., Wood, 2000), indicating that condensate in small drizzle drops contributes significantly to r_e in UCL clouds and therefore influences significantly the optical properties of UCL clouds.

b. Turbulence

Clouds in UCLs tend to be much less turbulent than non-UCL clouds in the same altitude range. Fig. 6 shows estimates of inertial range turbulence derived every second using windowed (1 Hz) vertical velocity variance (σ_w^2) from the high frequency (25 Hz) vertical wind measurements. Cloudy UCLs typically have mean σ_w^2 from 0.015-0.03 m^{2}s^{-2}, whereas cloudy samples that are

non UCLs have values 3-5 times higher than this. This difference is consistent at all longitudes (not shown). Differences for clear samples are weaker, as are the turbulence levels themselves. Above 1 km altitude, clear UCLs have turbulence levels close to the likely minimum value that can be accurately determined with the aircraft turbulence probe (roughly 0.005 m^2 s^{-2}). In the altitude range 0.5-1.5 km, non UCL clear regions have trubulence levels roughly 30-100% higher than UCL clear regions, but above 1.5 km the differences are smaller. Thus, it may be concluded that both clear and cloudy UCLs, are typically significantly more quiescent than non-UCL equivalents at similar levels. There are likely some important consequences of low turbulence levels in UCLs. First, a UCL that mixes with air either above or below would typically result in an increase in aerosol concentration in the layer. Second, introduction of drier air via turbulent mixing into a saturated, cloudy UCL would also tend to result in cloud dessication. The low turbulence levels observed in UCLs, and the implied suppression of vertical mixing, therefore probably helps to explain their high frequency of occurrence. It may also be indicative of the process by which UCLs are formed in the first place. Theoretical and observational evidence suggests that Cu clouds detrain air preferentially at levels where there is static stability in the environmental profile (Raymond and Blyth, 1986; Bretherton and Smolarkiewicz, 1988; Perry and Hobbs, 1996; Zuidema, 1998). If UCL clouds are predominantly formed in this way, then one would expect suppressed turbulence as the rising parcels in the cumulus encountered regions of increased buoyancy, causing deceleration of vertical motion. Visual evidence of a rather laminar appearance of many of the layer clouds observed in CSET is presented in section 5.

5. Case studies

The statistical analysis of the properties of UCLs determined using *in situ* aircraft observations reveals that both cloudy and clear UCLs are common, especially in the upper parts of the marine

PBL above the surface mixed layer. In this section, we combine these observations with aircraft and satellite remote sensing information to provide additional context to highlight properties of UCL clouds that are difficult to ascertain using *in situ* data alone.

a. 29 July 2015, Research Flight 11

On 29 July 2015, CSET RF11 returned from Hilo to Sacramento and flew for 11 minutes (19:37-19:48 UTC) through the upper levels of an aggregated cumulus cluster situated at 29°N, 145°W approximately 1500 km to the northwest of Hawaii. Fig. 7(a) shows visible satellite imagery of the cluster indicating the track that the G-V flew through the system, while Fig. 7(b,c) show photographs indicating extensive quasi-laminar layer clouds at a level similar to that of the aircraft ($\sim$2750 m). Just before exiting the cluster at 19:47 the G-V climbed slightly to an altitude of 3350 m. The G-V passed through both clear and cloudy UCLs, as indicated by N_a and N_d concentrations (green and dark blue dots respectively in Fig. 7(d)) below 10 cm^{-3}. Unfortunately, the UHSAS instrument suffered overheating during the period shown, but total aerosol concentrations N_{CN} sampled in clear layers from 19:39-19:47 UTC after the UHSAS overheated remained very low and in the range 10-30 cm^{-3} (red dots in Fig. 7(d)), indicating likely clear UCLs associated with the high relative humidity air. In the dry free tropospheric air prior to the aircraft overflying the cluster (19:36-19:37) and after the overpass (19:47-19:48) there was a marked increase in aerosol concentrations, indicating that the source of the sampled UCLs in this case is associated with the humid air in the upper reaches of the cumulus cluster.

Lidar backscatter imagery from the HSRL below the aircraft (Fig. 7(e)) indicates the presence of numerous horizontally-extensive cloud layers with top altitudes ranging from 1.5-2.5 km. Perhaps half of the cloud layers with tops around 1.5-2.0 km attenuate the lidar, but many do not. Those layers above 2 km rarely attenuated the lidar despite some of them (e.g., those from 19:42-

19:44 UTC) being as thick as 1 km. We refer to these thin clouds overlying the cumulus cluster as *veil clouds*. The G-V passed through the tops of these optically thin cloud layers from 19:41-19:43 UTC and measured condensate consisting of both cloud drops and small drizzle-sized drops (measured with the CDP and 2DC respectively). Total condensate amounts ranged from 0.04-0.1 g m^{-3} (Fig. 7(d)). Measured N_d in these UCL clouds was typically 1-3 cm^{-3} with effective radii ranging from 20-50 μm (cyan dots in Fig. 7(d)). Despite relatively low condensate loadings, most of the UCL clouds detected by the lidar here produced detectable radar echoes with reflectivities in the range -15 to -25 dBZ (Fig. 7(f)), consistent with significant condensate loading in the form of drizzle drops. Thus, in this case and in many others not shown here, the optically thin veil clouds are mostly existing in UCLs.

A remarkable feature of the optically thin veil clouds sampled in this cluster, given that they contain appreciable drizzle-sized drops, is that many have very sharply defined bases (seen in the HSRL and HCR images and also in the photographs in Fig. 7) with little evidence of virga in most cases, other than in some of the most geometrically thick but optically thin layer clouds (e.g., 19:43-19:44). This suggests that many of the veil clouds may not simply be decaying remnants of precipitating layers but may be being actively maintained. Evidence for mesoscale lofting of PBL air within aggregated trade cumulus clusters is found in large eddy simulations (Bretherton and Blossey, 2017), where such vertical motion appears to be supported by circulations that develop between the suppressed regions surrounding clusters and the active clusters themselves. How such mesoscale ascent, and how the UCL cloud microphysics might each impact cloud cover and longevity of veil clouds are questions worthy of further inquiry.

Although in this case we do not have an G-V profile to provide vertical context, a decoupled PBL structure is evident throughout the sampling period. This is clearest before 19:37 and after 19:44 UTC when there is a relatively strongly scattering surface mixed layer extending up to 1 km

overlain with layers of much lower scattering. In places (e.g., at 2.5 km altitude from 19:36-19:39, and just below 1.5 km altitude between 19:44-19:45 UTC) there are curious horizontally-extensive layers of increased lidar scattering. It is possible that these layers are caused by the evaporation of cloud droplets (the scattering layers are horizontally adjacent to cloud layers).

In addition to the qualitative information provided by the lidar and radar sensors on the G-V, a real strength of these instruments is in their combination with each other to produce quantitative retrievals of cloud properties. The radar-lidar sensor synergy is at its best for the optically thin veil clouds, where lidar backscatter is available throughout the cloud layer. Fig. 8 shows retrievals of liquid water content and droplet effective radius using a variant of the O'Connor et al. (2005) method (Schwartz and Ghate, 2017), for the same 29 July cloud case shown in Fig. 7. Retrieved liquid water contents range up to 0.5 g m^{-3} are found, especially lower down in the cloud layer below the level of the G-V. Effective radii exceeding 20 μm are found in much of the cloud layer, yielding estimates of cloud droplet concentration N_d that are a few cm^{-3}, and in good agreement with *in situ* estimates (Fig. 8d). In this study, we show only this one case, but future work could include a systematic analysis of the lidar-radar retrievals from all the CSET flights to help quantify their frequency, liquid water path and droplet concentration.

b. 27 July 2015, Research Flight 10

On 27 July 2015, CSET RF10 flew from Sacramento to Hilo and sampled large clusters of aggregated cumulus convection and associated veil clouds west of the Sc-Cu transition (138°W). A time lapse set of GOES visible imagery illustrates the temporal evolution of optically thin veil clouds (reflectances of $\sim$0.2) and demonstrates their relationship with bright (reflectances exceeding 0.4) Cu clouds (Fig. 9). In this case, the G-V flew a straight leg through a stratiform cloud at the top of the PBL ($\sim$2300 m). Low cloud droplet concentrations measured with the G-V were in the UCL

range during the latter half of the leg (Fig. 10c). Effective radii exceeds 20 μm over much of this leg (Fig. 10), even reaching as high as 40-60 μm. MODIS-retrieved cloud droplet effective radii are also very high over a large fraction of the cloud system (Fig. 10b) with independent estimates from the combined CDP/2D-C and HOLODEC in excellent agreement (Fig. 10d).

The temporal evolution seen in the GOES imagery is particularly revealing, as it demonstrates several key aspects the lifecycle of veil clouds. Active Cu clouds appear to be necessary for the initial formation of the stratiform veil clouds (Cu without veil clouds develop them after 1-3 hours as seen in Fig. 9e-h). After the active Cu weaken and dissipate (e.g., Fig. 9e-g), the veil clouds persist for a few more hours but then eventually evaporate (Fig. 9h,i). In this case there was relatively little vertical shear of the horizontal wind within the PBL, and the veil cloud locations remain quite close to the Cu that produce them. However, in other cases with directional wind shear in the PBL, veil clouds in the upper PBL can move in a direction opposite to the direction of motion of the Cu, and this sometimes leaves isolated patches of optically thin veil clouds completely disconnected from the Cu that generated them in the first place. Fig. 9g also demonstrates that aggregated Cu clusters are associated with rather large increases in column water vapor (from 25 mm in the suppressed regions to as high as 40 mm in the Cu patches). This concentration of moisture in the regions of active Cu appears to be a typical feature of shallow convective self-aggregation, as indicated by large domain large eddy simulations (Bretherton and Blossey, 2017).

c. 19 July 2015, Research Flight 7

The failure rate for visible/near infrared (VIS/NIR) cloud optical property retrievals from NASA's Moderate Resolution Imaging Spectroradiometer (MODIS) is approximately 10% Cho et al. (2015). The most prevalent type of failure of, explaining 60-85% of all failed retrievals, is

that the cloud effective radius implied by the combination of visible and NIR channels is larger than the upper bound (30 μm) in the look-up table Cho et al. (2015). The mean UCL cloud effective radus determined using *in situ* cloud probe data is $\sim$20 μm (Fig. 4d), but that effective radii frequently approach and sometimes exceed 30 μm (see part II of this paper, O et al. (2017)). Given this, the failure of MODIS retrievals due the presence of large droplets should not be surprising.

Here, we examine data from CSET Research Flight 7 on 19 July 2015, and compare *in situ* and satellite retrieved cloud properties, in this case from the GOES-15 geostationary satellite. Photographic and satellite observations show intermingled shallow cumulus convection and stratiform veil clouds during the G-V traverse through an exensive field of open cellular clouds on a return leg from Hawaii to Sacramento (Fig. 11a-c). The aircraft remained within clouds with similar open cellular morphology from 152°W to 135°W, a distance of over 1700 km sampled over approximately four hours (18:10-22:15 UTC). During this period the aircraft made numerous cloud penetrations, and GOES-15 cloud product retrievals (using a combination of 0.63 and 3.9 μm wavelength channels, Minnis et al., 2008a,b, 2011) were processed for the 17 images (15 minute temporal resolution) obtained during the aircraft sampling period. Retrievals from all pixels within a 2° swath around the aircraft track were used to produce histograms of cloud droplet concentration (Painemal et al., 2015) and effective radius for the transect that are compared with those derived from the *in situ* data (Fig. 11d,e). Although there is a rather large scale mismatch between the aircraft *in situ* microphysical estimates and those from the rather coarse ($\sim$4 km) GOES pixels, the two estimates agree fairly well, with median droplet concentrations N_d of 7 cm^{-3} (GOES) and 5 cm^{-3} (*in situ*), and median effective radii of 24 μm (GOES) and 21 μm (*in situ*). The histograms do show some differences, with larger tails seen in the *in situ* data, which may be symptomatic of the different spatial scales of the measurements, but in general the agreement between the aircraft and satellite retrievals are rather good. This is somewhat surprising because these open cellular

regions do contain a significant fraction of clouds that are not particularly well-suited to VIS/NIR satellite retrievals, which assume plane parallel clouds, and may suffer from ambiguity problems for clouds of low optical thickness. Despite this, these findings provide some encouragement that passive satellite retrievals in such aggregated cumulus clusters may not be as poor as has sometimes been supposed, especially if the retrievals are used statistically to characterize the average microphysical properties of cloud systems rather than at the pixel level.

Examination of effective radius images from GOES-15 in the region (e.g., Fig. 11b) indicates that extensive regions of the northeastern Pacific are typically covered with clouds with effective radii of 25-30 μm at any one time, a finding consistent with our observations documenting the frequent occurrence of UCL clouds in the region. Thus, it is likely that even if the quantitative accuracy of the GOES-15 retrievals is poor, the estimates may still serve as a useful means to identify and track cloudy ultra-clean layers. Further work detailing more extensive comparisons of aircraft and satellite data will be needed to ascertain the extent to which this is the case.

6. Aircraft remote sensing of optically thin clouds

As can be readily seen in Fig. 7, a rather high fraction of the clouds sampled in CSET do not fully attenuate the HSRL lidar beam. The HSRL-determined cloud mask (Schwartz and Ghate, 2017) identifies clouds detected by the HSRL and also provides a flag indicating whether the beam has been attenuated. We use all zenith-pointing data from the near-surface level legs (see section 2a) to ensure that HSRL has a view of the entire column and therefore can determine the low cloud cover. For each lidar profile, we first determine if low clouds are present using the cloud mask. Here, low clouds are defined as those with HSRL-detected bases below 3 km altitude. These data can be used to determine the overall low cloud cover. Then, profiles that contain low cloud are separated into three categories: (i) optically thick low clouds, which are those profiles containing

a single low cloud layer that fully attenuates the lidar beam; (ii) a single layer of optically thin low cloud, i.e., a low cloud that does not fully attenuate the lidar, determined by detecting a lidar signal from above the cloud layer; (iii) multiple layers of low clouds. This latter category could contain multiple optically thin low cloud layers, or optically thin low cloud layers below optically thick low cloud layer above. For the single layer optically thin cloud we are able to determine both the cloud layer base and the top, and thus the cloud thickness.

Cloud statistics from all CSET flights are aggregated into 5° longitude bins from 125-155°W (Fig. 12). Consistent with existing satellite climatologies (e.g., Karlsson et al., 2010; Leahy et al., 2012), low cloud cover decreases moving westward as the MBL transitions from relatively shallow at the location of the stratocumulus maximum around 130-135°W to a deeper MBL close to Hawaii. Low cloud cover decreases as the MBL deepens and the stratocumulus-cumulus transition occurs. The fraction of low clouds that are optically thin increases westward from below 0.4 east of 135°W to 0.6-0.7 west of 140°W. These high values are consistent with CALIPSO lidar based climatologies (Leahy et al., 2012; Guzman et al., 2017). We further subdivide the optically thin low clouds into those occurring in the upper MBL (bases at or above 1 km altitude) that we refer to as veil clouds ($f_{low,thin,z>1km}$) and those with bases near the lifting condensation level (bases below 700 m altitude, $f_{low,thin,z<700m}$). Fig. 12 shows that most of the optically thin low clouds observed in CSET occurred in the upper PBL above 1 km, and are therefore considered veil clouds. Optically thin LCL clouds are far less numerous and nowhere contribute more than 15% of all optically thin low clouds. The increasing frequency of optically thin low clouds moving westwards mirrors the increase in frequency of both clear and cloudy UCLs (Fig. 3), consistent with other lines of evidence indicating a tight connection between strongly depleted layers and the occurrence of optically thin veil clouds.

The heights and thicknesses of all the optically thin cloud layers detected by the zenith-pointing HSRL during CSET are summarized in Fig. 13. The figure shows box-whisker plots showing geometrical thickness vs cloud base height, with the blue curve providing the cumulative frequency of cloud base height. The median cloud base height of the optically thin clouds is 1150 m, with 10th and 90th percentiles of 625 m and 1700 m respectively. Mean geometrical thicknesses of the optically thin layers are just over 200 m (medians are a little lower, $\sim$180 m), with little evidence of a systematic variation of thickness as base height increases. Some optically thick layers are as thick as 300-400 m; the optically thin clouds shown in Fig. 7 exceed this thickness in places. Most optically thin clouds are therefore occurring in the upper PBL above the surface mixed layer, whose top is typically 600-700 m. The height distribution of the fraction of cloudy samples that are UCLs determined using *in situ* data (Fig. 2) also shows few UCLs in the surface mixed layer, and a rapid increase with height, which is consistent with the idea that many optically thin low clouds are also UCL clouds. The red dashed line in Fig. 13 shows the cumulative distribution of the heights of UCL clouds determined using the *in situ* G-V cloud probe data. It should be stressed, however, that the cumulative frequency distribution of the heights of UCL clouds may be biased by non uniform height sampling by the G-V. To attempt to mitigate this potential sampling bias, we normalized the number of cloudy UCL samples identified at each level by the total number of aircraft samples at each level. The cumulative distributions of the lidar-determined optically thin cloud base height and the *in situ* determined UCL cloud height are similar, providing additional evidence of a close connection between optically thin clouds and UCL clouds. The two cumulative distributions do diverge somewhat at heights above about 1200 m, with almost twice as many cloudy UCLs occurring above 1500 m than optically thin clouds.

7. Discussion

They two key findings in this paper are that (a) ultraclean layers are a frequent occurrence in the MBL in the stratocumulus to cumulus transition region of the northeastern subtropical Pacific Ocean; (b) many clouds in UCLs tend to be optically thin, quasi-laminar stratiform veil clouds containing large droplets but relatively low liquid water contents. These clouds tend to occur in the upper part of the decoupled trade wind PBL and are only infrequently found in the surface mixed layer below 600 m or so. Veil clouds are particularly common in cases of open mesoscale cellular convection and in large ($\sim$100 km wide) aggregated cumulus clusters. The tendency for a high frequency of optically thin clouds in open and disorganized cellular convection has been previously observed (see, e.g., the cloud optical thickness distributions shown in Fig. 14 in Muhlbauer et al. (2014)) but their microphysical and detailed structural properties have not been previously described. Veil clouds tend to be geometrically as well as optically thin, and so their low optical thickness can be attributed to a combination of their thinness and their very low droplet concentrations (optical thickness scales with $N_d^{\frac{1}{3}}$). Veil clouds are relatively free of turbulence, and so assume a laminar like structure when viewed from the side. In the heart of the SCT upwind of Hawaii, the aircraft observations suggest that $\sim$50% of cloudy columns contain UCL clouds, and a similar fraction of low clouds is optically thin in this region, again consistent with the idea that most veil clouds are severely depleted of droplets. This begs the question of how UCL/veil clouds are formed, how they are maintained, how they eventually dissipate and what aerosol they leave behind upon evaporation. Visible geostationary imagery over a period of several hours demonstrates that veil clouds tend to form 1-2 hours after the formation of bright, active Cu cloud clusters, and then persist for roughly the same amount of time once the active Cu weaken and disappear. Although we have not conducted an exhaustive study of veil cloud

lifetimes, the veil clouds examined here last for several hours in total. Thus, veil clouds are a common feature of aggregated cumulus patches, and likely consistute the majority of the cloud cover within these patches.

a. What determines the lifecycle and microphysics of UCLs and veil clouds?

In Part II of this paper (O et al., 2017) we use microphysical parcel modeling to explore the idea that UCL clouds are created by rapid removal of cloud droplets by collision-coalescence in the moist updrafts of the active Cu clouds in aggregated clusters or in open cells, so that when these Cu detrain saturated air, it is already strongly depleted in droplets. This detrainment mechanism for UCL cloud formation appears to capture some key microphysical properties of UCL clouds, and can explain their longitudinal variation within the stratocumulus to cumulus transition, but other hypotheses may also explain them. For example, if aggregated Cu clusters are regions of weak mesoscale ascent, as is suggested in large eddy simulations (e.g., Bretherton and Blossey, 2017) then it might be possible for UCLs to form *in situ* rather than from detrainment of condensate from the more active Cu towers. However, if this were the case, then it is difficult to explain how the accumulation mode aerosol concentrations N_a in clear UCLs can have formed. Slow ascent on the order of $\sim$1 cm s^{-1} (as found in the simulations of Bretherton and Blossey (2017) in the aggregated Cu clusters) would indeed tend to result in rather low N_d even when N_a exceeds the UCL threshold of 10 cm^{-3}. However, such a cloud would also contain a significant number of interstitial unactivated accumulation mode aerosol that would remain in place after the cloud dissipated. Thus, it is difficult to explain the frequent occurrence of clear UCLs with such a formation mechanism. Mesoscale ascent could, by providing condensate, enhance veil cloud longevity compared with a case with no mesoscale ascent, and may help to explain their observed lifetimes of several hours. The terminal velocity of cloud droplets increases for 1.2 cm s^{-1} for

droplets with radii of 10 μm to 5 cm s^{-1} for droplets with radii of 20 μm, indicating that sustained mesoscale ascent of several cm s^{-1} would be required to maintain a UCL cloud against dessication by sedimentation of droplets out of the layer. Whether such mesoscale lofting occurs for a sufficiently long time within aggregated cumulus clusters warrants further study using large domain cloud resolving models. It is possible that size sorting of droplets occurs in UCL clouds over the cloud lifecycle, such that the largest droplets are removed by sedimentation out of the cloud base, leaving behind smaller droplets. This temporal evolution of UCL cloud microphysics is explored in Part II of this paper.

b. Condensate loading and optical thickness of veil clouds

Based on the measurements presented here, we can make a first attempt to quantify the mean condensate loading contained in veil clouds in the SCT. First, we note the mean veil cloud liquid water contents (sum of the CDP and 2DC liquid water contents) are $\sim$0.12 g m^{-3} (Fig. 4c). It is worth noting that an uncertain, but likely significant fraction of the condensate is contained in small drizzle-sized drops larger than the CDP upper limit (25 μm radius) but smaller than the first reliable bin of the 2DC (37.5 μm radius), so this condensate loading may be a lower limit. Next, we found that the mean geometrical thickness of veil clouds is just over 200 m (Fig. 13). The product of the mean veil cloud liquid water content and the geometrical thickness yields an estimate of the mean liquid water path (LWP) of approximately 25 g m^{-2}, which is significant, although it should be pointed out that this LWP is close to the detection limit for passive microwave retrievals (Wentz, 1997), making accurate spaceborne quantification of condensate loading in veil clouds challenging.

Cloud optical thickness (see e.g., George and Wood, 2010) is related to LWP and N_d via

$$\tau \approx K N_d^{\frac{1}{3}} LW P^{\frac{5}{6}} \quad (1)$$

where K is a weak function of temperature and pressure and $K \sim 0.25$ kg$^{-5/6}$ m^3 for $T = 280$ K and $p = 850$ hPa. For the typical veil cloud LWP of 25 g m^{-2} and $N_d \sim 5$ cm^{-3} (Fig. 4a), yielding $\tau \sim 2$. This low value of τ is consistent with the frequent penetration of veil clouds by the lidar. If veil clouds did not have such low N_d, but instead had values close to the accumulation model aerosol in the surface mixed layer ($\sim$75 cm^{-3}, see part II of this paper), then from Eqn. 1, $\tau \sim 5$, in which case lidar would not penetrate the cloud. Indeed, for a threshold optical depth of 3 below which lidar will penetrate (Winker and Poole, 1995), N_d must be below approximately 20 cm^{-3}. Thus, the low optical thickness of veil clouds is strongly contingent on their low droplet concentrations. Given the frequent occurrence of veil clouds, this implies that there may be a direct control of regional cloud albedo by precipitation through coalescence scavenging.

c. On the radiative susceptibility of veil clouds

CSET data show that many UCL clouds, despite being optically and geometrically thin, have radar echoes significantly higher than -30 dBZ such that they can be detected with the W-band radar on the G-V aircraft and may even be detectable and characterizable using spaceborne radar. Radar-lidar retrievals designed originally for quantification of the microphysical properties of drizzle show considerable promise for remote characterization of the microphysical properties, condensate loadings, and potentially the albedo susceptibility of veil clouds to changes in aerosol loading. The relatively low albedo A of veil clouds does not drastically reduce their albedo susceptiblity to changes in droplet concentration N_d, which scales as $dA/dN_d = A(1-A)/3N_d$ (Platnick and Twomey, 1994), and thus is only about one third lower for $A = 0.2$ compared with $A = 0.5$.

On the other hand, the extremely low N_d in UCL clouds implies a very high albedo susceptibility (Twomey effect). Marine low clouds shoulder a large fraction of the global indirect aerosol forcing in climate models (e.g., Kooperman et al., 2012; Carslaw et al., 2013; Lee et al., 2016), so it is important to understand whether models have the appropriate albedo susceptibility given the tendency for large scale models to produce an insufficient fraction of optically thin clouds. That said, the albedo susceptibility defined by Platnick and Twomey (1994) does not deal with the extent to which N_d *can* be perturbed by increases in anthropogenic aerosol emissions. For MBL clouds over the remote oceans, the pathways by which N_d can be increased is either via increased marine shipping emissions (surface sources) or by the entrainment of long-range transported polluted air from the FT. But in order to perturb veil cloud N_d, surface air must first pass through cumulus clouds in order to reach the upper MBL. Coalescence scavenging in cumulus updrafts is likely to strongly limit the perturbation to veil cloud N_d that would be expected from a given increase in aerosol loading in the surface mixed layer. Thus, although veil clouds have high albedo susceptibility, microphysical processes driving their production may limit their ability to realize this susceptibility. Further, because veil clouds tend to be quiescent, their ability to entrain FT air and tap into the higher aerosol concentrations there may also be strongly limited too. Exploring the degree to which veil clouds can be perturbed by aerosol is an important topic for further study.

Beyond the Twomey effect, there is the question of whether the colloidal stability of low N_d veil clouds may change if aerosol loadings increase. Answering this will require much greater understanding of the lifecycle of veil clouds and of the factors that control their coverage and lifetime. An additional aspect of the susceptibility of top of atmosphere radiation to changes in the optical thickness or coverage of veil clouds is that they likely have significant longwave cloud radiative effects by virtue of their temperature contrast with the surface and because emissivity is sensitive to droplet effective radius for typical UCL cloud droplet sizes (Wood, 2012).

d. Outlook for future research

Over the global oceans, roughly half of all low clouds do not fully attenuate spaceborne lidar Leahy et al. (2012), indicating the important contribution of optically thin MBL clouds to global cloud cover, especially in the subtropics and tropics. Less is known about the contribution of these clouds to the overall cloud radiative effect. In the SCT regions, these optically thin clouds comprise a mixture of small fair weather trade cumulus clouds with bases typically tied to the lifting condensation level (LCL), and much more horizontally extensive stratiform veil-type clouds that reside in the upper MBL. Quantifying the contribution of each of these types of optically thin cloud to cloud cover and to overall radiative effect is a significant challenge, but one that can probably be largely achieved with current and planned active spaceborne remote sensing technology. Understanding of the large-scale conditions that encourage/discourage UCL production is needed. As major a challenge is to accurately represent veil clouds and UCLs in large-scale numerical models and to understand how they may change in response to increasing greenhouse gases and to aerosol changes. Parameterizations that are able to treat cumulus convection and stratiform veil clouds as tightly coupled entities with strongly interacting microphysical and macrophysical processes are likely to bear most fruit.

Acknowledgments. The authors are extremely grateful to the staff, aircrew, and groundcrew of the Research Aviation Facility at the National Center for Atmospheric Research who operated the G-V aircraft used in this study. We would like to thank the instrument scientists and operators who worked tirelessly to provide high-quality datasets used here. Financial support for the analysis presented here is from the National Science Foundation (Grant AGS-1445813).

References

Ackerman, A. S., 2003: Enhancement of cloud cover and suppression of nocturnal drizzle in stratocumulus polluted by haze. *Geophysical Research Letters*, **30 (7)**, doi:10.1029/2002GL016634, URL http://doi.wiley.com/10.1029/2002GL016634.

Albrecht, B., 2017: Cloud System Evolution in the Trades (CSET) Field Campaign.

Augstein, E., H. Riehl, F. Ostapoff, and V. Wagner, 1973: Mass and Energy Transports in an Undisturbed Atlantic Trade-Wind Flow. *Mon. Wea. Rev.*, **101 (2)**, 101–111, doi:10.1175/1520-0493(1973)101⟨0101:MAETIA⟩2.3.CO;2, URL http://journals.ametsoc.org.offcampus.lib.washington.edu/doi/10.1175/1520-0493%281973%29101%3C0101%3AMAETIA%3E2.3.CO%3B2.

Berner, A. H., C. S. Bretherton, R. Wood, and A. Muhlbauer, 2013: Marine boundary layer cloud regimes and POC formation in a CRM coupled to a bulk aerosol scheme. *Atmospheric Chemistry and Physics*, **13 (24)**, 12 549–12 572, doi:10.5194/acp-13-12549-2013, URL http://www.atmos-chem-phys.net/13/12549/2013/.

Bodas-Salcedo, A., and Coauthors, 2014: Origins of the Solar Radiation Biases over the Southern Ocean in CFMIP2 Models*. *Journal of Climate*, **27 (1)**, 41–56, doi:10.1175/JCLI-D-13-00169.1, URL http://journals.ametsoc.org/doi/abs/10.1175/JCLI-D-13-00169.1.

Bretherton, C. S., P. Austin, and S. T. Siems, 1995: Cloudiness and Marine Boundary Layer Dynamics in the ASTEX Lagrangian Experiments. Part II: Cloudiness, Drizzle, Surface Fluxes, and Entrainment. *J. Atmos. Sci.*, **52 (16)**, 2724–2735, doi:10.1175/1520-0469(1995)052⟨2724:CAMBLD⟩2.0.CO;2, URL http://journals.ametsoc.org/doi/abs/10.1175/1520-0469%281995%29052%3C2724%3ACAMBLD%3E2.0.CO%3B2.

Bretherton, C. S., and P. Blossey, 2017: Understanding mesoscale aggregation of shallow cumulus convection using large-eddy simulation.

Bretherton, C. S., and R. Pincus, 1995: Cloudiness and Marine Boundary Layer Dynamics in the ASTEX Lagrangian Experiments. Part I: Synoptic Setting and Vertical Structure. *J. Atmos. Sci.*, **52 (16)**, 2707–2723, doi:10.1175/1520-0469(1995)052⟨2707:CAMBLD⟩2.0.CO;2, URL http://journals.ametsoc.org/doi/abs/10.1175/1520-0469%281995%29052%3C2707%3ACAMBLD%3E2.0.CO%3B2.

Bretherton, C. S., and P. Smolarkiewicz, 1988: Gravity Waves, Compensating Subsidence and Detrainment around Cumulus Clouds. *J. Atmos. Sci.*, **46 (6)**, 740–759, doi:10.1175/1520-0469(1989)046⟨0740:GWCSAD⟩2.0.CO;2, URL http://journals.ametsoc.org.offcampus.lib.washington.edu/doi/citedby/10.1175/1520-0469%281989%29046%3C0740%3AGWCSAD%3E2.0.CO%3B2.

Bretherton, C. S., and M. C. Wyant, 1997: Moisture transport, lower-tropospheric stability, and decoupling of cloud-topped boundary layers. *Journal of the atmospheric sciences*, **54 (1)**, 148–167, URL http://journals.ametsoc.org/doi/full/10.1175/1520-0469(1997)054%3C0148:MTLTSA%3E2.0.CO%3B2.

Carslaw, K. S., and Coauthors, 2013: Large contribution of natural aerosols to uncertainty in indirect forcing. *Nature*, **503 (7474)**, 67–71, doi:10.1038/nature12674, URL http://www.nature.com/doifinder/10.1038/nature12674.

Cho, H.-M., and Coauthors, 2015: Frequency and causes of failed MODIS cloud property retrievals for liquid phase clouds over global oceans: FAILED MODIS CLOUD RETRIEVALS. *Journal of Geophysical Research: Atmospheres*, **120 (9)**, 4132–4154, doi:10.1002/2015JD023161, URL http://doi.wiley.com/10.1002/2015JD023161.

Engstrm, A., F. a.-M. Bender, R. J. Charlson, and R. Wood, 2015: The nonlinear relationship between albedo and cloud fraction on near-global, monthly mean scale in observations and in the CMIP5 model ensemble. *Geophys. Res. Lett.*, **42 (21)**, 2015GL066 275, doi:10.1002/2015GL066275, URL http://onlinelibrary.wiley.com.offcampus.lib.washington.edu/doi/10.1002/2015GL066275/abstract.

Field, P. R., R. J. Cotton, K. McBeath, A. P. Lock, S. Webster, and R. P. Allan, 2014: Improving a convection-permitting model simulation of a cold air outbreak: Simulation of a Cold Air Outbreak. *Quarterly Journal of the Royal Meteorological Society*, **140 (678)**, 124–138, doi:10.1002/qj.2116, URL http://doi.wiley.com/10.1002/qj.2116.

Fugal, J. P., and R. A. Shaw, 2009: Cloud particle size distributions measured with an airborne digital in-line holographic instrument. *Atmos. Meas. Tech.*, **2 (1)**, 259–271, doi:10.5194/amt-2-259-2009, URL http://www.atmos-meas-tech.net/2/259/2009/.

George, R. C., and R. Wood, 2010: Subseasonal variability of low cloud radiative properties over the southeast Pacific Ocean. *Atmospheric Chemistry and Physics*, **10 (8)**, 4047–4063, doi:10.5194/acp-10-4047-2010, URL http://www.atmos-chem-phys.net/10/4047/2010/.

Grund, C. J., and E. W. Eloranta, 1991: University of Wisconsin High Spectral Resolution Lidar. *Opt. Eng*, **30 (1)**, 6–12, doi:10.1117/12.55766, URL http://dx.doi.org/10.1117/12.55766.

Guzman, R., and Coauthors, 2017: Direct atmosphere opacity observations from CALIPSO provide new constraints on cloud-radiation interactions: GOCCP v3.0 OPAQ Algorithm. *Journal of Geophysical Research: Atmospheres*, doi:10.1002/2016JD025946, URL http://doi.wiley.com/10.1002/2016JD025946.

Hindman, E. E., W. M. Porch, J. G. Hudson, and P. A. Durkee, 1994: Ship-produced cloud lines of 13 July 1991. *Atmospheric Environment*, **28 (20)**, 3393–3403, doi:10.1016/1352-2310(94)00171-G, URL http://www.sciencedirect.com/science/article/pii/135223109400171G.

Hobbs, P. V., 2003: Clean air slots amid dense atmospheric pollution in southern Africa. *J. Geophys. Res.*, **108 (D13)**, 8490, doi:10.1029/2002JD002156, URL http://onlinelibrary.wiley.com/doi/10.1029/2002JD002156/abstract.

Hudson, J. G., and Y. Xie, 1999: Vertical distributions of cloud condensation nuclei spectra over the summertime northeast Pacific and Atlantic Oceans. *J. Geophys. Res.*, **104 (D23)**, 30 219–30 229, doi:10.1029/1999JD900413, URL http://onlinelibrary.wiley.com.offcampus.lib.washington.edu/doi/10.1029/1999JD900413/abstract.

Karlsson, J., G. Svensson, S. Cardoso, J. Teixeira, and S. Paradise, 2010: Subtropical Cloud-Regime Transitions: Boundary Layer Depth and Cloud-Top Height Evolution in Models and Observations. *J. Appl. Meteor. Climatol.*, **49 (9)**, 1845–1858, doi:10.1175/2010JAMC2338.1, URL http://journals.ametsoc.org/doi/abs/10.1175/2010JAMC2338.1.

Kazil, J., H. Wang, G. Feingold, A. D. Clarke, J. R. Snider, and A. R. Bandy, 2011: Modeling chemical and aerosol processes in the transition from closed to open cells during VOCALS-REx. *Atmos. Chem. Phys.*, **11 (15)**, 7491–7514, doi:10.5194/acp-11-7491-2011, URL http://www.atmos-chem-phys.net/11/7491/2011/.

Kooperman, G. J., M. S. Pritchard, S. J. Ghan, M. Wang, R. C. J. Somerville, and L. M. Russell, 2012: Constraining the influence of natural variability to improve estimates of global aerosol indirect effects in a nudged version of the Community Atmosphere Model 5. *Journal of Geophysical Research*, **117 (D23)**, doi:10.1029/2012JD018588, URL http://doi.wiley.com/10.1029/2012JD018588.

Krueger, S. K., G. T. McLean, and Q. Fu, 1995: Numerical Simulation of the Stratus-to-Cumulus Transition in the Subtropical Marine Boundary Layer. Part II: Boundary-Layer Circulation. *J. Atmos. Sci.*, **52 (16)**, 2851–2868, doi:10.1175/1520-0469(1995)052⟨2851:NSOTST⟩2.0.CO;2, URL http://journals.ametsoc.org.offcampus.lib.washington.edu/doi/abs/10.1175/1520-0469%281995%29052%3C2851%3ANSOTST%3E2.0.CO%3B2.

Leahy, L. V., R. Wood, R. J. Charlson, C. A. Hostetler, R. R. Rogers, M. A. Vaughan, and D. M. Winker, 2012: On the nature and extent of optically thin marine low clouds: OPTICALLY THIN MARINE LOW CLOUDS. *Journal of Geophysical Research: Atmospheres*, **117 (D22)**, n/a–n/a, doi:10.1029/2012JD017929, URL http://doi.wiley.com/10.1029/2012JD017929.

Lee, L. A., C. L. Reddington, and K. S. Carslaw, 2016: On the relationship between aerosol model uncertainty and radiative forcing uncertainty. *PNAS*, **113 (21)**, 5820–5827, doi:10.1073/pnas.1507050113, URL http://www.pnas.org/content/113/21/5820.

Lu, M.-L., W. C. Conant, H. H. Jonsson, V. Varutbangkul, R. C. Flagan, and J. H. Seinfeld, 2007: The Marine Stratus/Stratocumulus Experiment (MASE): Aerosol-cloud relationships in marine stratocumulus. *Journal of Geophysical Research*, **112 (D10)**, doi:10.1029/2006JD007985, URL http://doi.wiley.com/10.1029/2006JD007985.

Martin, G. M., D. W. Johnson, D. P. Rogers, P. R. Jonas, P. Minnis, and D. A. Hegg, 1995: Observations of the Interaction between Cumulus Clouds and Warm Stratocumulus Clouds in the Marine Boundary Layer during ASTEX. *J. Atmos. Sci.*, **52 (16)**, 2902–2922, doi:10.1175/1520-0469(1995)052⟨2902:OOTIBC⟩2.0.CO;2, URL http://journals.ametsoc.org.offcampus.lib.washington.edu/doi/abs/10.1175/1520-0469(1995)052%3C2902:OOTIBC%3E2.0.CO;2.

Martin, G. M., D. W. Johnson, and A. Spice, 1994: The Measurement and Parameterization of Effective Radius of Droplets in Warm Stratocumulus Clouds. *J. At-*

mos. Sci., **51 (13)**, 1823–1842, doi:10.1175/1520-0469(1994)051⟨1823:TMAPOE⟩2.0.CO;2, URL http://journals.ametsoc.org/doi/abs/10.1175/1520-0469%281994%29051%3C1823%3ATMAPOE%3E2.0.CO%3B2.

Mauritsen, T., and Coauthors, 2011: An Arctic CCN-limited cloud-aerosol regime. *Atmospheric Chemistry and Physics*, **11 (1)**, 165–173, doi:10.5194/acp-11-165-2011, URL http://www.atmos-chem-phys.net/11/165/2011/.

Miles, N. L., J. Verlinde, and E. E. Clothiaux, 2000: Cloud droplet size distributions in low-level stratiform clouds. *Journal of the atmospheric sciences*, **57 (2)**, 295–311, URL http://journals.ametsoc.org/doi/abs/10.1175/1520-0469(2000)057%3C0295:CDSDIL%3E2.0.CO%3B2.

Miller, M. A., and B. A. Albrecht, 1995: Surface-Based Observations of Mesoscale CumulusStratocumulus Interaction during ASTEX. *J. Atmos. Sci.*, **52 (16)**, 2809–2826, doi:10.1175/1520-0469(1995)052⟨2809:SBOOMC⟩2.0.CO;2, URL http://journals.ametsoc.org.offcampus.lib.washington.edu/doi/abs/10.1175/1520-0469%281995%29052%3C2809%3ASBOOMC%3E2.0.CO%3B2.

Minnis, P., and Coauthors, 2008a: Cloud Detection in Nonpolar Regions for CERES Using TRMM VIRS and Terra and Aqua MODIS Data. *IEEE Transactions on Geoscience and Remote Sensing*, **46 (11)**, 3857–3884, doi:10.1109/TGRS.2008.2001351.

Minnis, P., and Coauthors, 2008b: Near-real time cloud retrievals from operational and research meteorological satellites. Vol. 7107, 710 703–710 703–8, doi:10.1117/12.800344, URL http://dx.doi.org/10.1117/12.800344.

Minnis, P., and Coauthors, 2011: CERES Edition-2 Cloud Property Retrievals Using TRMM VIRS and Terra and Aqua MODIS Data #x2014;Part I: Algorithms. *IEEE Transactions on Geo-*

science and Remote Sensing, **49 (11)**, 4374–4400, doi:10.1109/TGRS.2011.2144601.

Morcrette, J.-J., and Y. Fouquart, 1986: The Overlapping of Cloud Layers in Shortwave Radiation Parameterizations. *J. Atmos. Sci.*, **43 (4)**, 321–328, doi:10.1175/1520-0469(1986)043⟨0321:TOOCLI⟩2.0.CO;2, URL http://journals.ametsoc.org/doi/abs/10.1175/1520-0469%281986%29043%3C0321%3ATOOCLI%3E2.0.CO%3B2.

Muhlbauer, A., I. L. McCoy, and R. Wood, 2014: Climatology of stratocumulus cloud morphologies: microphysical properties and radiative effects. *Atmospheric Chemistry and Physics*, **14 (13)**, 6695–6716, doi:10.5194/acp-14-6695-2014, URL http://www.atmos-chem-phys.net/14/6695/2014/.

Nam, C., S. Bony, J.-L. Dufresne, and H. Chepfer, 2012: The too few, too bright tropical low-cloud problem in CMIP5 models. *Geophys. Res. Lett.*, **39 (21)**, L21 801, doi:10.1029/2012GL053421, URL http://onlinelibrary.wiley.com/doi/10.1029/2012GL053421/abstract.

O, K.-T., R. Wood, and C. S. Bretherton, 2017: Ultraclean layers and optically thin clouds in the stratocumulus to cumulus transition. Part II: Depletion of cloud droplets and cloud condensation nuclei through collision-coalescence in marine boundary layer clouds. *J. Atmos. Sci*, submitted.

O'Connor, E. J., R. J. Hogan, and A. J. Illingworth, 2005: Retrieving stratocumulus drizzle parameters using Doppler radar and lidar. *Journal of Applied Meteorology*, **44 (1)**, 14–27, URL http://journals.ametsoc.org/doi/abs/10.1175/JAM-2181.1.

Painemal, D., P. Minnis, and M. Nordeen, 2015: Aerosol variability, synoptic-scale processes, and their link to the cloud microphysics over the northeast Pacific during MAGIC: NE PACIFIC CCN AND CLOUD MICROPHYSICS. *Journal of Geophysical Research: Atmo-*

spheres, **120 (10)**, 5122–5139, doi:10.1002/2015JD023175, URL http://doi.wiley.com/10.1002/2015JD023175.

Perry, K., and P. V. Hobbs, 1996: Influences of Isolated Cumulus Clouds on the Humidity of Their Surroundings. *J. Atmos. Sci.*, **53 (1)**, 159–174, doi:10.1175/1520-0469(1996)053⟨0159:IOICCO⟩2.0.CO;2, URL http://journals.ametsoc.org/doi/abs/10.1175/1520-0469(1996)053%3C0159:IOICCO%3E2.0.CO;2.

Petters, M. D., J. R. Snider, B. Stevens, G. Vali, I. Faloona, and L. M. Russell, 2006: Accumulation mode aerosol, pockets of open cells, and particle nucleation in the remote subtropical Pacific marine boundary layer. *J. Geophys. Res.*, **111 (D2)**, D02 206, doi:10.1029/2004JD005694, URL http://onlinelibrary.wiley.com.offcampus.lib.washington.edu/doi/10.1029/2004JD005694/abstract.

Platnick, S., and S. Twomey, 1994: Determining the Susceptibility of Cloud Albedo to Changes in Droplet Concentration with the Advanced Very High Resolution Radiometer. *J. Appl. Meteor.*, **33 (3)**, 334–347, doi:10.1175/1520-0450(1994)033⟨0334:DTSOCA⟩2.0.CO;2, URL http://journals.ametsoc.org/doi/abs/10.1175/1520-0450(1994)033%3C0334:DTSOCA%3E2.0.CO;2.

Raymond, D. J., and A. M. Blyth, 1986: A Stochastic Mixing Model for Non-precipitating Cumulus Clouds. *J. Atmos. Sci.*, **43 (22)**, 2708–2718, doi:10.1175/1520-0469(1986)043⟨2708:ASMMFN⟩2.0.CO;2, URL http://journals.ametsoc.org/doi/abs/10.1175/1520-0469(1986)043%3C2708:ASMMFN%3E2.0.CO;2.

Sandu, I., and B. Stevens, 2011: On the Factors Modulating the Stratocumulus to Cumulus Transitions. *Journal of the Atmospheric Sciences*, **68 (9)**, 1865–1881, doi:10.1175/2011JAS3614.1, URL http://journals.ametsoc.org/doi/abs/10.1175/2011JAS3614.1.

Sandu, I., B. Stevens, and R. Pincus, 2010: On the transitions in marine boundary layer cloudiness. *Atmospheric Chemistry and Physics*, **10 (5)**, 2377–2391, URL http://www.atmos-chem-phys.net/10/2377/.

Schwartz, C., and V. Ghate, 2017: Retrievals of cloud and precipitation using airborne lidar-radar data from the northeastern Pacific. *Journal of Atmospheric and Oceanic Technology*.

Sharon, T. M., B. A. Albrecht, H. H. Jonsson, P. Minnis, M. M. Khaiyer, T. M. van Reken, J. Seinfeld, and R. Flagan, 2006: Aerosol and cloud microphysical characteristics of rifts and gradients in maritime stratocumulus clouds. *Journal of the atmospheric sciences*, **63 (3)**, 983–997, URL http://journals.ametsoc.org/doi/abs/10.1175/JAS3667.1.

Stevens, B., G. Vali, K. Comstock, R. Wood, M. C. Van Zanten, P. H. Austin, C. S. Bretherton, and D. H. Lenschow, 2005: POCKETS OF OPEN CELLS AND DRIZZLE IN MARINE STRATOCUMULUS. *Bulletin of the American Meteorological Society*, **86 (1)**, 51–57, doi:10.1175/BAMS-86-1-51, URL http://journals.ametsoc.org/doi/abs/10.1175/BAMS-86-1-51.

Stevens, B., and Coauthors, 2001: Simulations of Trade Wind Cumuli under a Strong Inversion. *J. Atmos. Sci.*, **58 (14)**, 1870–1891, doi:10.1175/1520-0469(2001)058⟨1870:SOTWCU⟩2.0.CO;2, URL http://journals.ametsoc.org.offcampus.lib.washington.edu/doi/abs/10.1175/1520-0469(2001)058%3C1870:SOTWCU%3E2.0.CO;2.

Teixeira, J., and Coauthors, 2011: Tropical and Subtropical Cloud Transitions in Weather and Climate Prediction Models: The GCSS/WGNE Pacific Cross-Section Intercomparison (GPCI). *J. Climate*, **24 (20)**, 5223–5256, doi:10.1175/2011JCLI3672.1, URL http://journals.ametsoc.org.offcampus.lib.washington.edu/doi/abs/10.1175/2011JCLI3672.1.

Terai, C. R., C. S. Bretherton, R. Wood, and G. Painter, 2014: Aircraft observations of aerosol, cloud, precipitation, and boundary layer properties in pockets of open cells over the southeast Pacific. *Atmospheric Chemistry and Physics*, **14 (15)**, 8071–8088, doi:10.5194/acp-14-8071-2014, URL http://www.atmos-chem-phys.net/14/8071/2014/.

Vivekanandan, J., and Coauthors, 2015: A wing pod-based millimeter wavelength airborne cloud radar. *Geoscientific Instrumentation, Methods and Data Systems*, **4 (2)**, 161–176, doi:10.5194/gi-4-161-2015, URL http://www.geosci-instrum-method-data-syst.net/4/161/2015/.

Wentz, F. J., 1997: A well-calibrated ocean algorithm for special sensor microwave / imager. *J. Geophys. Res.*, **102 (C4)**, 8703–8718, doi:10.1029/96JC01751, URL http://onlinelibrary.wiley.com.offcampus.lib.washington.edu/doi/10.1029/96JC01751/abstract.

Williams, K. D., and Coauthors, 2012: The Transpose-AMIP II Experiment and Its Application to the Understanding of Southern Ocean Cloud Biases in Climate Models. *J. Climate*, **26 (10)**, 3258–3274, doi:10.1175/JCLI-D-12-00429.1, URL http://journals.ametsoc.org/doi/abs/10.1175/JCLI-D-12-00429.1.

Winker, D. M., and L. R. Poole, 1995: Monte-Carlo calculations of cloud returns for ground-based and space-based LIDARS. *Appl. Phys. B*, **60 (4)**, 341–344, doi:10.1007/BF01082269, URL https://link.springer.com/article/10.1007/BF01082269.

Wood, R., 2000: Parametrization of the effect of drizzle upon the droplet effective radius in stratocumulus clouds. *Q.J.R. Meteorol. Soc.*, **126 (570)**, 3309–3324, doi:10.1002/qj.49712657015, URL http://onlinelibrary.wiley.com/doi/10.1002/qj.49712657015/abstract.

Wood, R., 2012: Stratocumulus Clouds. *Monthly Weather Review*, **140 (8)**, 2373–2423, doi:10.1175/MWR-D-11-00121.1, URL http://journals.ametsoc.org/doi/abs/10.1175/

MWR-D-11-00121.1.

Wood, R., C. S. Bretherton, D. Leon, A. D. Clarke, P. Zuidema, G. Allen, and H. Coe, 2011: An aircraft case study of the spatial transition from closed to open mesoscale cellular convection over the Southeast Pacific. *Atmos. Chem. Phys.*, **11 (5)**, 2341–2370, doi:10.5194/acp-11-2341-2011, URL http://www.atmos-chem-phys.net/11/2341/2011/.

Wood, R., K. K. Comstock, C. S. Bretherton, C. Cornish, J. Tomlinson, D. R. Collins, and C. Fairall, 2008: Open cellular structure in marine stratocumulus sheets. *Journal of Geophysical Research*, **113 (D12)**, doi:10.1029/2007JD009371, URL http://doi.wiley.com/10.1029/2007JD009371.

Wood, R., D. Leon, M. Lebsock, J. Snider, and A. D. Clarke, 2012: Precipitation driving of droplet concentration variability in marine low clouds: PRECIPITATION DRIVING OF DROP CONC. *Journal of Geophysical Research: Atmospheres*, **117 (D19)**, n/a–n/a, doi:10.1029/2012JD018305, URL http://doi.wiley.com/10.1029/2012JD018305.

Wyant, M. C., C. S. Bretherton, H. A. Rand, and D. E. Stevens, 1997: Numerical simulations and a conceptual model of the stratocumulus to trade cumulus transition. *Journal of the atmospheric sciences*, **54 (1)**, 168–192, URL http://journals.ametsoc.org/doi/abs/10.1175/1520-0469(1997)054%3C0168%3ANSAACM%3E2.0.CO%3B2.

Zhou, X., P. Kollias, and E. R. Lewis, 2015: Clouds, Precipitation, and Marine Boundary Layer Structure during the MAGIC Field Campaign. *J. Climate*, **28 (6)**, 2420–2442, doi:10.1175/JCLI-D-14-00320.1, URL http://journals.ametsoc.org/doi/abs/10.1175/JCLI-D-14-00320.1.

Zuidema, P., 1998: The 600800-mb Minimum in Tropical Cloudiness Observed during TOGA COARE. *J. Atmos. Sci.*, **55 (12)**, 2220–2228, doi:10.1175/1520-0469(1998)055⟨2220:

973 TMMITC⟩2.0.CO;2, URL http://journals.ametsoc.org/doi/abs/10.1175/1520-0469%281998%
974 29055%3C2220%3ATMMITC%3E2.0.CO%3B2.

LIST OF FIGURES

spectral resolution lidar (HSRL); (f) radar reflectivity factor curtain from the HIAPER cloud radar (HCR). 55

Fig. 8. Radar-lidar retrievals of veil cloud properties indicate a low number concentration of large drops. This case is the same transect shown in Fig. 7. Here, we show liquid water content and effective radius (upper two panels) retrieved using a modified form (Schwartz and Ghate, 2017) of the O'Connor et al. (2005) method that was designed initially to quantify drizzle properties falling below stratocumulus cloud bases. The aircraft flight altitude is shown with the thick solid line. The lower two panels show comparisons of *in situ* liquid water content and droplet number concentration N_d with the closest retrieval possible ($\sim$100 m below the aircraft). 56

Fig. 9. Evolution of active cumuli and veil clouds on 27 July (CSET RF10 flight) seen in GOES visible imagery over a period of eight hours. GOES visible imagery at $\sim$1 km resolution over a domain of approximately 3° longitude by 2° latitude that is advected westward with the G-V observed mean PBL wind. The G-V flew a straight leg through relatively optically thin veil clouds at 2250-2300 m altitude from 19:17-19:27 UTC (panel d), where cloud droplet concentration varied from 30-40 cm^{-3} during the first third of the leg (19:17-19:20 UTC) before dropping to values in the UCL range 1-10 cm^{-3} after 19:22 UTC (Fig. 10). The time-lapse imagery demonstrates that optically thin stratiform veil clouds form in regions adjacent to clusters of optically thick (active) cumulus clouds. Initially, bright Cu form without surrounding stratiform clouds, but veil clouds tend to develop 1-2 hours later (panel e and f). When the driving cumulus weaken and dissipate, as occurs after 20:30 UTC (panel e), the veil clouds persist for some hours before themselves dissipating (panel h and i). Panel g shows an overlay of the column water vapor from the AMSR-2 passive microwave imager on the GCOM-W1 satellite that flies in the A-Train. The GCOM-W1 overpass time of 22:25 UTC is almost coincident with the 22:30 GOES image and shows the the aggregated Cu clusters tend to be associated with quite large moisture perturbations. 57

Fig. 10. In situ and remotely sensed cloud microphysical properties near the top of the 27 July aggregated cumulus system shown in Fig. 9. *In situ* data shown here are from a section of the straight leg between 19:23 and 19:26 UTC (a horizontal distance of about 30 km). (a) a broad mean size distribution was observed by the cloud probes on the G-V, with the HOLODEC probe size distribution showing excellent agreement. The effective radius of this size distribution is 37 μm; (b) retrieved effective radius map (3.7 μm channel) from the MODIS instrument on the NASA Terra satellite showing prevalence of effective radii exceeding 25 μm. Note that retrievals of cloudy pixels with effective radii larger than 30 μm frequently fail (see section 5c) and constitute many of the gray regions; time series of (c) cloud droplet concentration N_d and (d) effective radius derived from the *in situ* CDP and 2D-C (circles) and from HOLODEC (blue line) showing excellent agreement. Effective radii as high as 40-60 μm are found in this system. 58

Fig. 11. Example of extensive patches of thin clouds associated with small cumulus clusters sampled by the G-V for over 1500 km (17:50-21:20 UTC) on flight RF07 on 19 July 2015. (a) a photograph from the left side of the aircraft at 18:25 UTC shows a cluster of bright Cu clouds interspersed with horizontally-extensive stratiform *veil* clouds; (b) satellite estimated cloud effective radius r_e from GOES-15 at 19:00 UTC (the white symbol on a circular black background shows the location of the photograph); (c) a visible GOES image at higher resolution of the region denoted by the box on the effective radius map showing trade Cu clusters in the form of loosely organized mesoscale open cells; the lower two panels show a statistical comparison of histograms of N_d (panel d) and r_e (panel e) from GOES-15 and from the G-V *in situ* data taken from the 1500 km portion of the G-V flight indicated by the

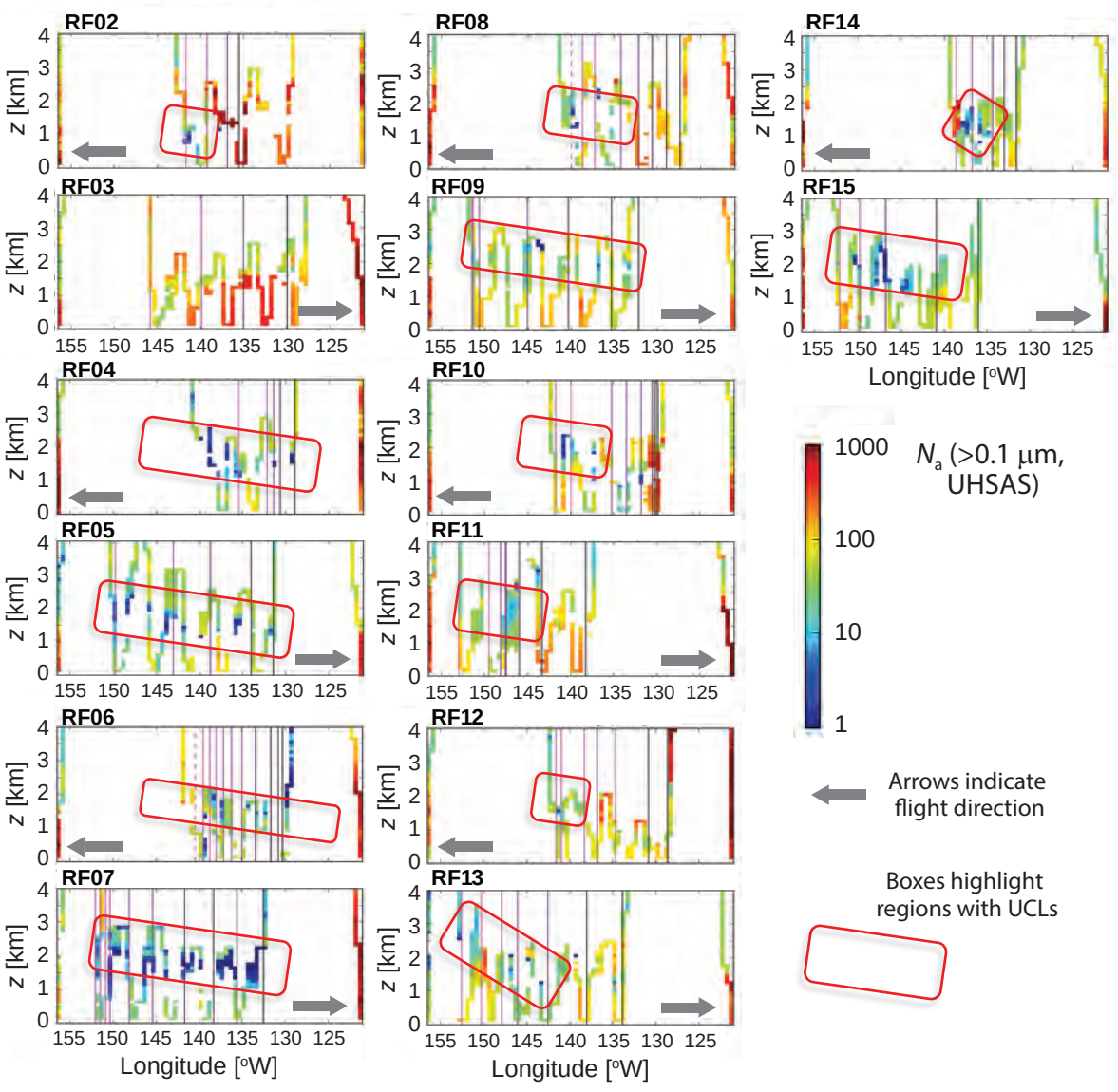

1093 FIG. 1. Longitude-height cross sections from CSET flights RF02 to RF15 showing the concentration N_a of
1094 aerosol particles larger than 0.1 μm (UHSAS) from all clear samples. Boxes highlight the presence of UCLs
1095 (blue colors). RFs 02, 04, 06, 08, 10, 12 and 14 are outbound (westward) flights, and RFs 03, 05, 07, 09,
1096 11, 13, 15 are the corresponding return (eastward) flights flown two days later. Thus RF02 and RF03 form a
1097 "mission pair" such that the RF03 flight plan was designed to resample approximately 48 hours later the air
1098 masses observed on RF02 advected using boundary layer trajectories as described in (Albrecht, 2017). The thin
1099 vertical lines show the longitudes of those air masses that were successfully sampled on both the outbound and
1100 return flights.

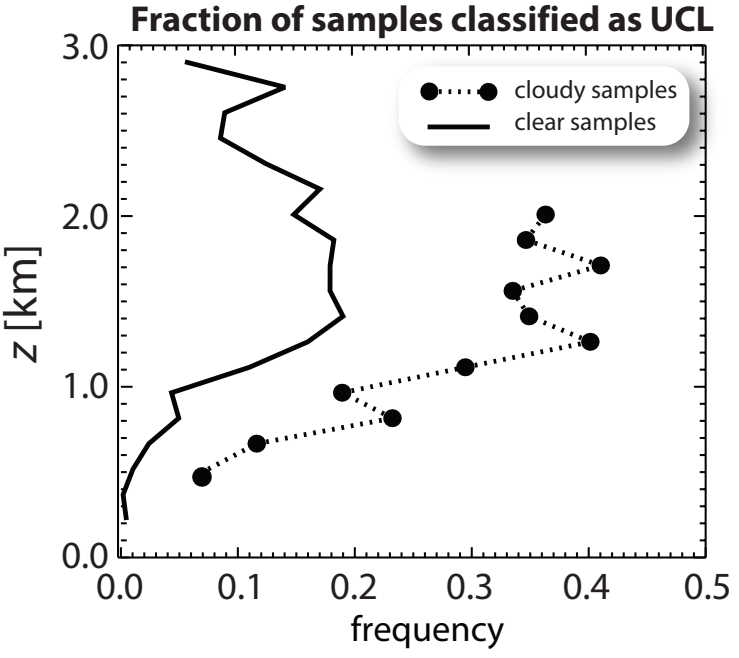

1101 FIG. 2. Vertical profile of the fraction of samples from the entire CSET campaign classified as UCLs broken
1102 down by whether the samples are clear or cloudy. Bins of 150 m altitude are used, and only those height levels
1103 containing at least thirty 1 Hz samples on each of three or more flights are shown.

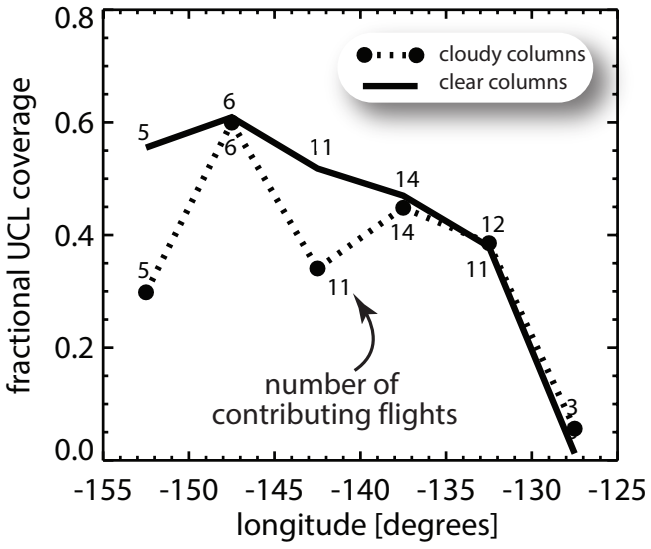

FIG. 3. Conditional probability (given cloudy or clear column) that column contains a UCL at some level (below 3 km) assuming maximum overlap. The number of flights contributing to each longitude bin's statistics is shown next to the data values.

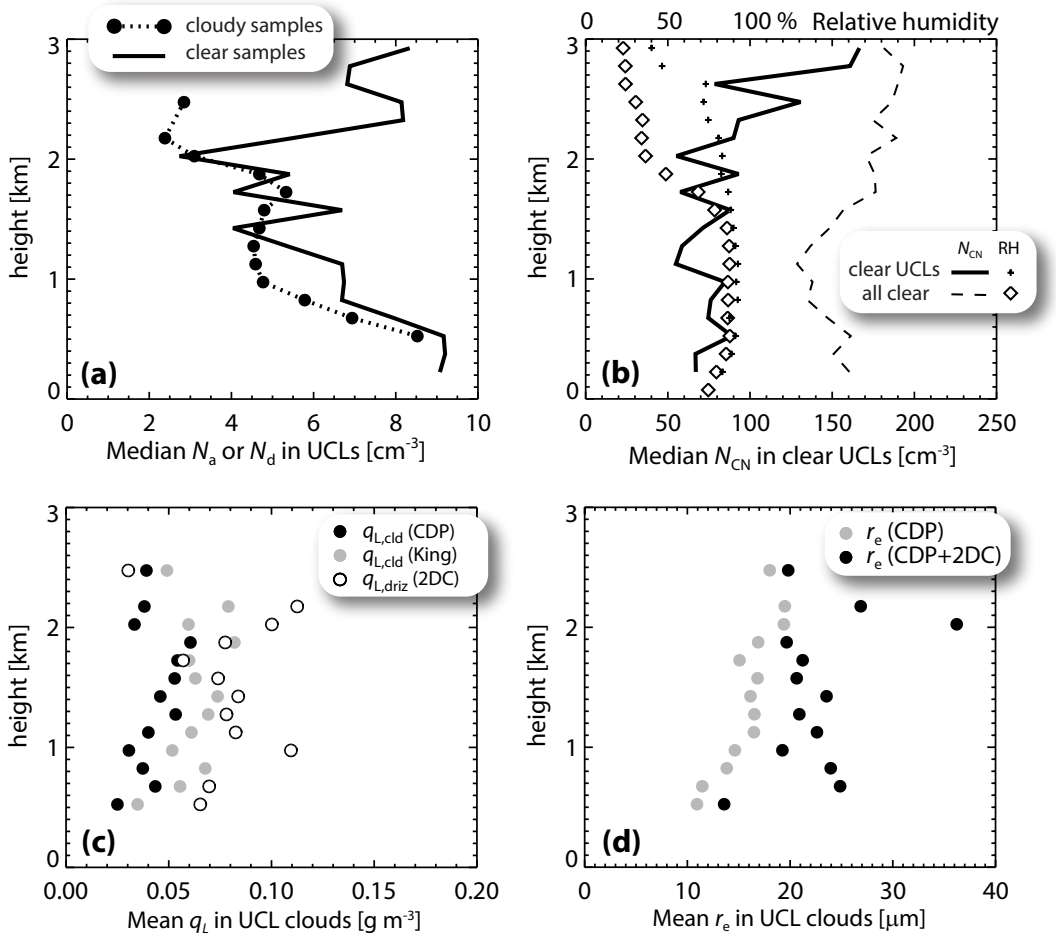

FIG. 4. Composite height-resolved properties of UCLs from G-V *in situ* measurements during CSET. (a) Median concentrations of aerosol particles larger than 0.1 μm (N_a) in clear UCLs (solid) and of cloud droplets (N_d) in UCL clouds, plotted as a function of UCL height; (b) Median condensation nucleus concentration (all particles larger than 10 nm) in clear UCLs (solid) and in all clear samples (dashed). Also shown is the mean relative humidity for UCLs (small crosses) and for all clear samples (diamonds); (c) Mean liquid water contents measured with different probes (black solid circles: CDP probe, droplets with radii smaller than 25 μm; gray solid circles: King hotwire probe; open circles: 2DC shadowprobe, measuring larger droplets with radii larger than 37.5 μm); (d) Mean cloud drop effective radius (r_e) considering only droplets with radii $<$25 μm (gray circles) and including all droplets (black circles).

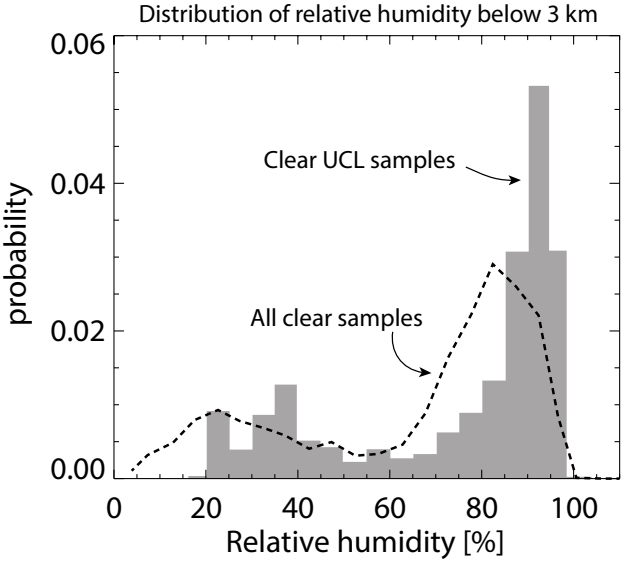

1116 FIG. 5. Probability distribution functions of clear sky relative humidity for all 1 Hz samples below 3 km
1117 (dashed line) and for all 1 Hz samples classified as clear UCLs (gray shading).

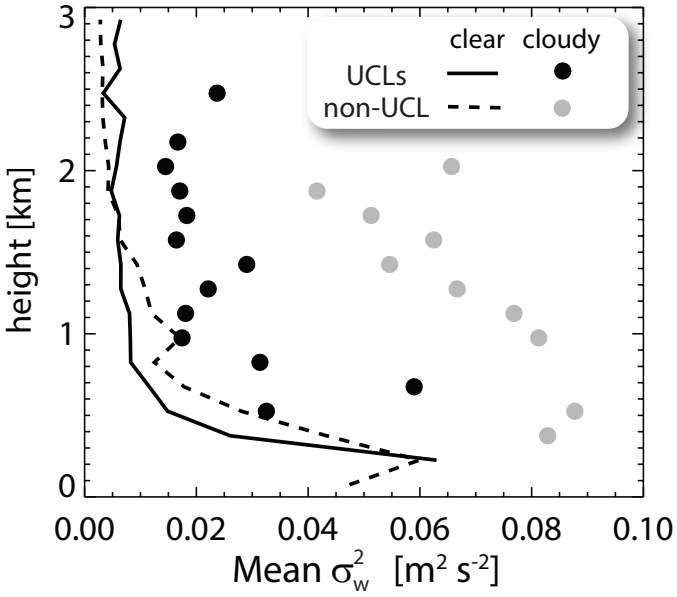

FIG. 6. Height resolved composite mean values of 1 Hz turbulent vertical wind variance for both cloudy (circles, black=UCL; gray=non UCL) and clear (solid=UCL; dashed=non UCL) samples from CSET.

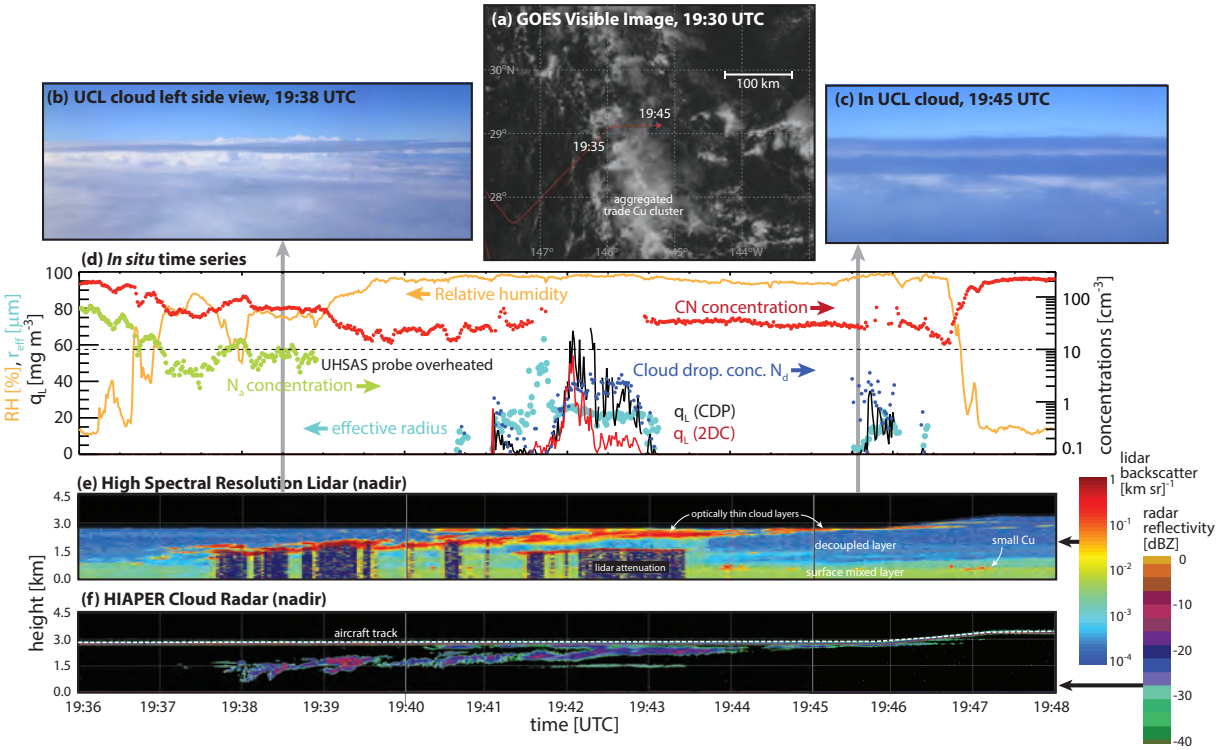

1120 FIG. 7. Case study of UCL cloud and clear layers sampled by the G-V between 19:36 and 19:48 during flight
1121 RF11 on 29 July 2015. (a) Visible satellite image from GOES-15 at 19:30 UTC showing aggregated Cu cluster
1122 approximately 100 km across along with the aircraft flight track (times marked on track); (b) photograph from
1123 the left side of the aircraft at 19:38 UTC showing bright Cu clouds and extensive layer (veil) cloud with gray
1124 appearance; (c) photograph taken during passage through optically thin UCL cloud at 19:45 UTC showing two-
1125 layered cloud structure at the level of the aircraft; (d) time series of several variables obtained using *in situ* G-V
1126 measurements during passage through system at 2.75 km altitude. Shown are concentrations of aerosol particles
1127 larger than 0.1 μm (N_a) (green, only available until 19:39 due to UHSAS overheating); CN concentration (red
1128 dots); N_d (blue dots); relative humidity (orange); liquid water content from the CDP (black line) and from the
1129 2DC (red line); effective radius (cyan); (e) lidar backscatter curtain below the aircraft from the high spectral
1130 resolution lidar (HSRL); (f) radar reflectivity factor curtain from the HIAPER cloud radar (HCR).

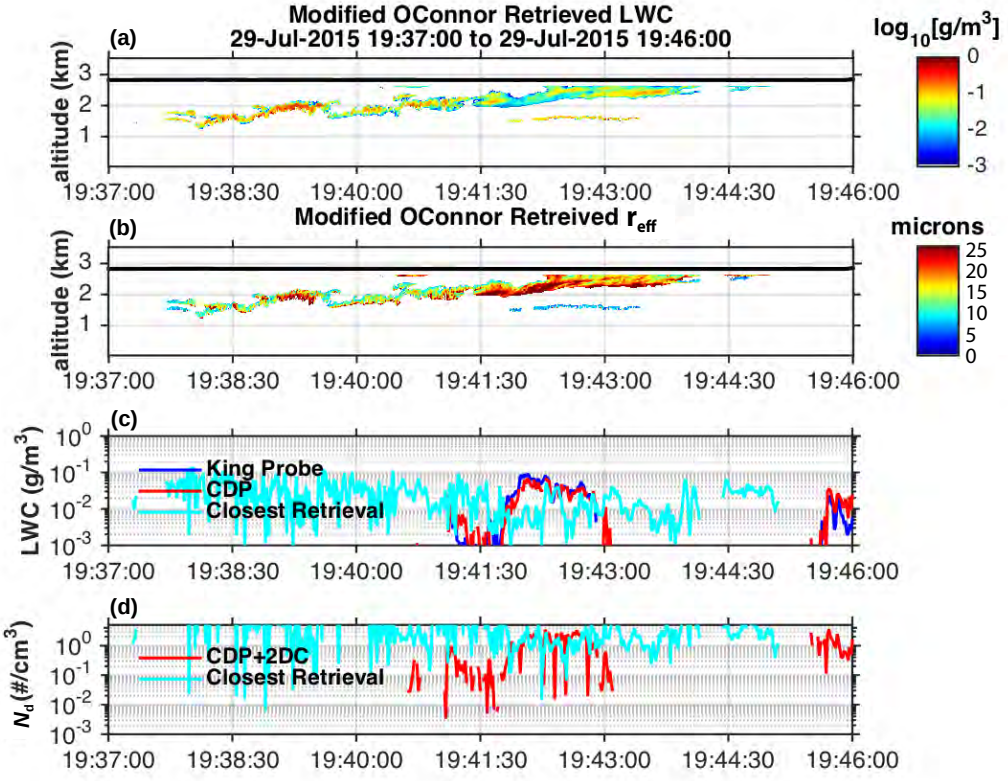

1131 FIG. 8. Radar-lidar retrievals of veil cloud properties indicate a low number concentration of large drops.
1132 This case is the same transect shown in Fig. 7. Here, we show liquid water content and effective radius (upper
1133 two panels) retrieved using a modified form (Schwartz and Ghate, 2017) of the O'Connor et al. (2005) method
1134 that was designed initially to quantify drizzle properties falling below stratocumulus cloud bases. The aircraft
1135 flight altitude is shown with the thick solid line. The lower two panels show comparisons of *in situ* liquid water
1136 content and droplet number concentration N_d with the closest retrieval possible ($\sim$100 m below the aircraft).

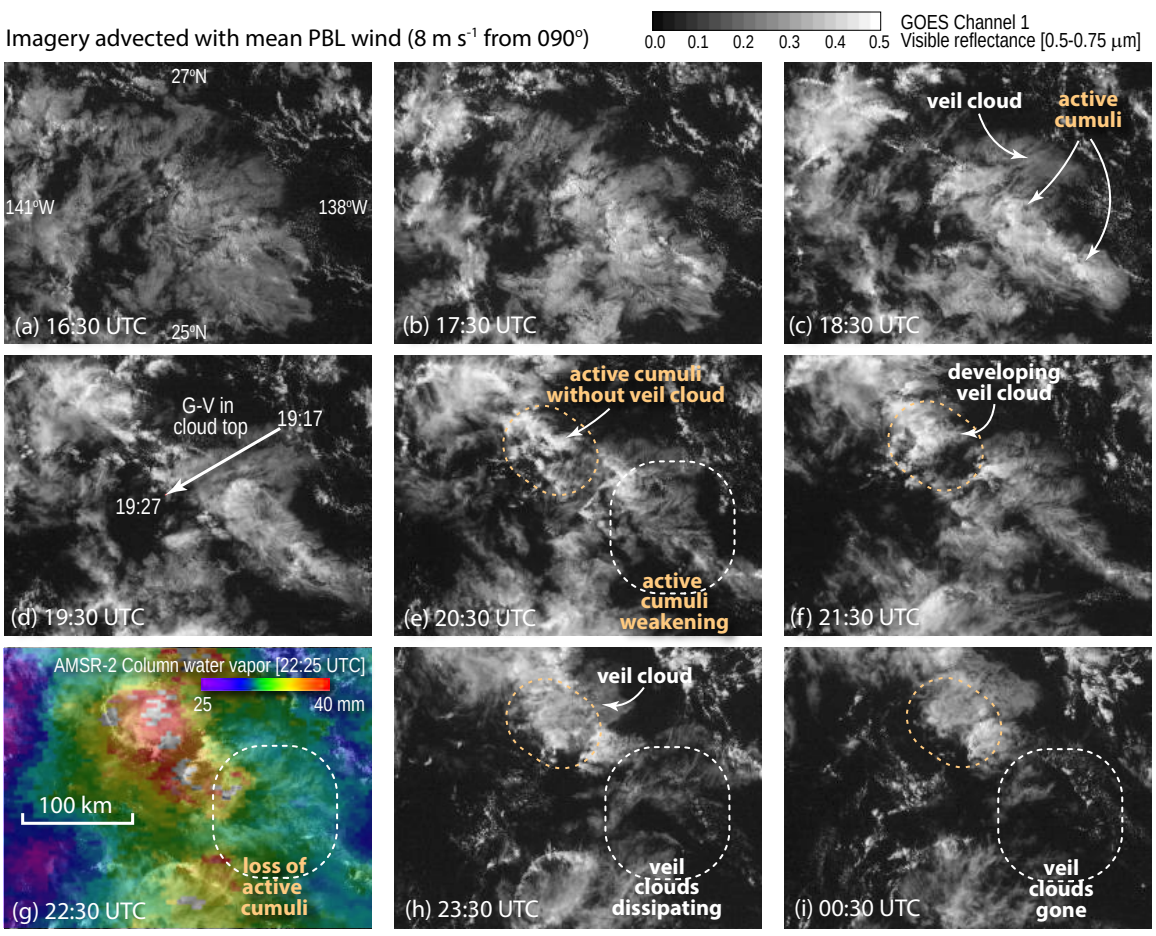

FIG. 9. Evolution of active cumuli and veil clouds on 27 July (CSET RF10 flight) seen in GOES visible imagery over a period of eight hours. GOES visible imagery at ∼1 km resolution over a domain of approximately 3° longitude by 2° latitude that is advected westward with the G-V observed mean PBL wind. The G-V flew a straight leg through relatively optically thin veil clouds at 2250-2300 m altitude from 19:17-19:27 UTC (panel d), where cloud droplet concentration varied from 30-40 cm^{-3} during the first third of the leg (19:17-19:20 UTC) before dropping to values in the UCL range 1-10 cm^{-3} after 19:22 UTC (Fig. 10). The time-lapse imagery demonstrates that optically thin stratiform veil clouds form in regions adjacent to clusters of optically thick (active) cumulus clouds. Initially, bright Cu form without surrounding stratiform clouds, but veil clouds tend to develop 1-2 hours later (panel e and f). When the driving cumulus weaken and dissipate, as occurs after 20:30 UTC (panel e), the veil clouds persist for some hours before themselves dissipating (panel h and i). Panel g shows an overlay of the column water vapor from the AMSR-2 passive microwave imager on the GCOM-W1 satellite that flies in the A-Train. The GCOM-W1 overpass time of 22:25 UTC is almost coincident with the 22:30 GOES image and shows the the aggregated Cu clusters tend to be associated with quite large moisture perturbations.

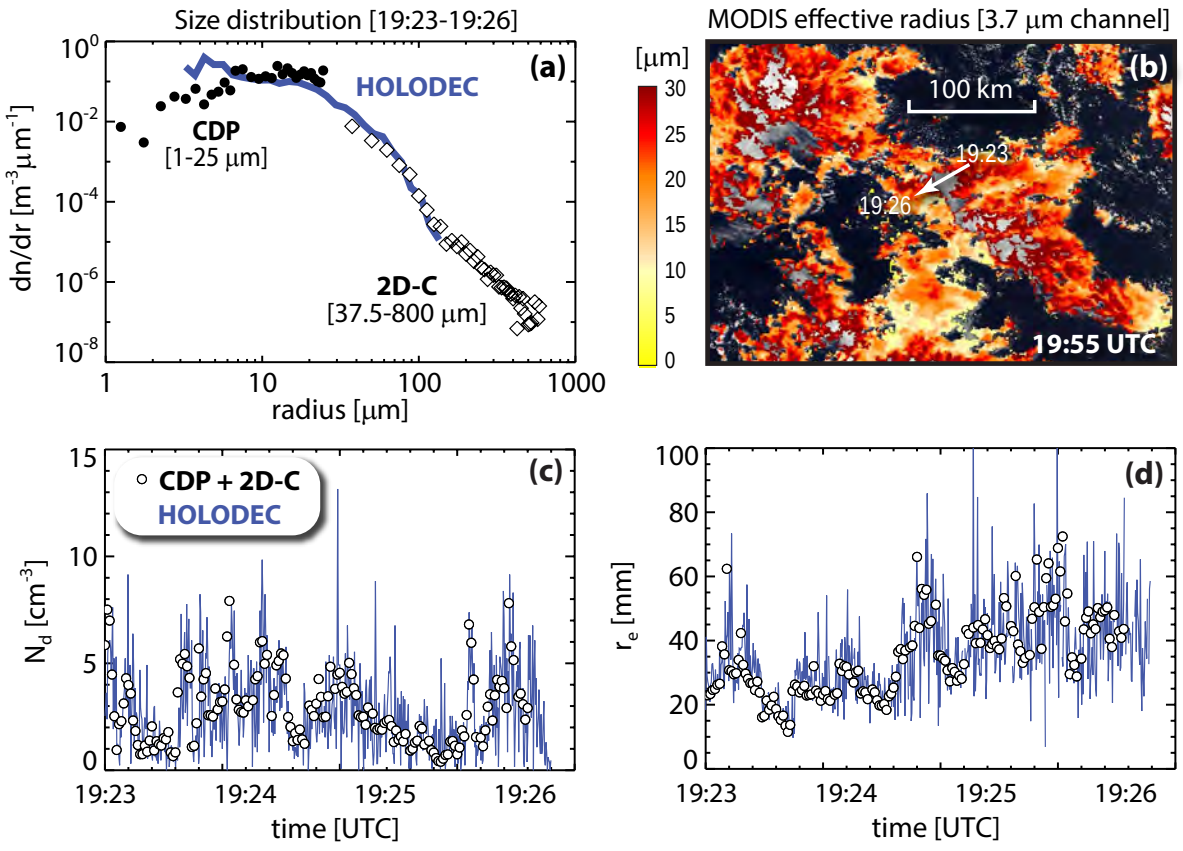

FIG. 10. In situ and remotely sensed cloud microphysical properties near the top of the 27 July aggregated cumulus system shown in Fig. 9. *In situ* data shown here are from a section of the straight leg between 19:23 and 19:26 UTC (a horizontal distance of about 30 km). (a) a broad mean size distribution was observed by the cloud probes on the G-V, with the HOLODEC probe size distribution showing excellent agreement. The effective radius of this size distribution is 37 μm; (b) retrieved effective radius map (3.7 μm channel) from the MODIS instrument on the NASA Terra satellite showing prevalence of effective radii exceeding 25 μm. Note that retrievals of cloudy pixels with effective radii larger than 30 μm frequently fail (see section 5c) and constitute many of the gray regions; time series of (c) cloud droplet concentration N_d and (d) effective radius derived from the *in situ* CDP and 2D-C (circles) and from HOLODEC (blue line) showing excellent agreement. Effective radii as high as 40-60 μm are found in this system.

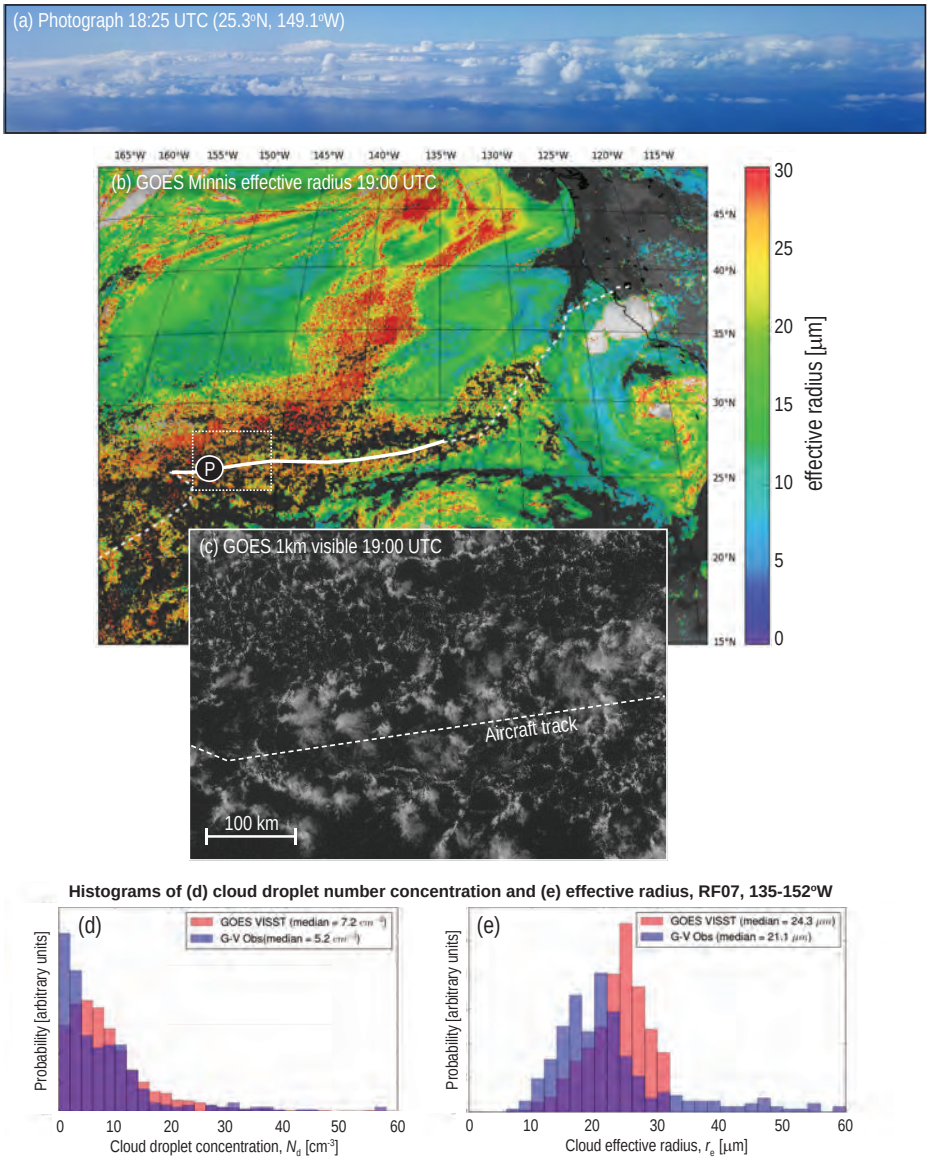

FIG. 11. Example of extensive patches of thin clouds associated with small cumulus clusters sampled by the G-V for over 1500 km (17:50-21:20 UTC) on flight RF07 on 19 July 2015. (a) a photograph from the left side of the aircraft at 18:25 UTC shows a cluster of bright Cu clouds interspersed with horizontally-extensive stratiform *veil* clouds; (b) satellite estimated cloud effective radius r_e from GOES-15 at 19:00 UTC (the white symbol on a circular black background shows the location of the photograph); (c) a visible GOES image at higher resolution of the region denoted by the box on the effective radius map showing trade Cu clusters in the form of loosely organized mesoscale open cells; the lower two panels show a statistical comparison of histograms of N_d (panel d) and r_e (panel e) from GOES-15 and from the G-V *in situ* data taken from the 1500 km portion of the G-V flight indicated by the thick solid line in (b) where the G-V was conducting low level sampling. See text for details of the data used to construct the histograms.

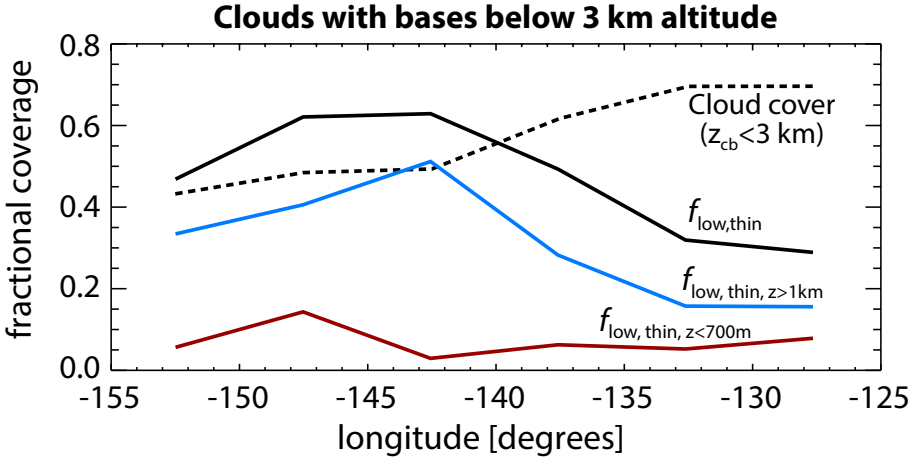

FIG. 12. Fraction of columns containing optically thin low clouds increases westward. Figure shows estimates from the HSRL in zenith-pointing mode on the G-V aircraft from near-surface level legs using the cloud mask of Schwartz and Ghate (2017). Only clouds with bases below 3 km are included. Dashed line: low cloud fractional cover from all clouds detected by the HSRL. Solid black line: fraction of low clouds that are optically thin, i.e. clouds detected by the HSRL that do not fully attenuate the lidar (see Leahy et al., 2012). Optically thin low clouds are further divided into clouds with bases above 1 km altitude (blue line) and those near the lifting condensation level ($z < 700$ m, red solid line).

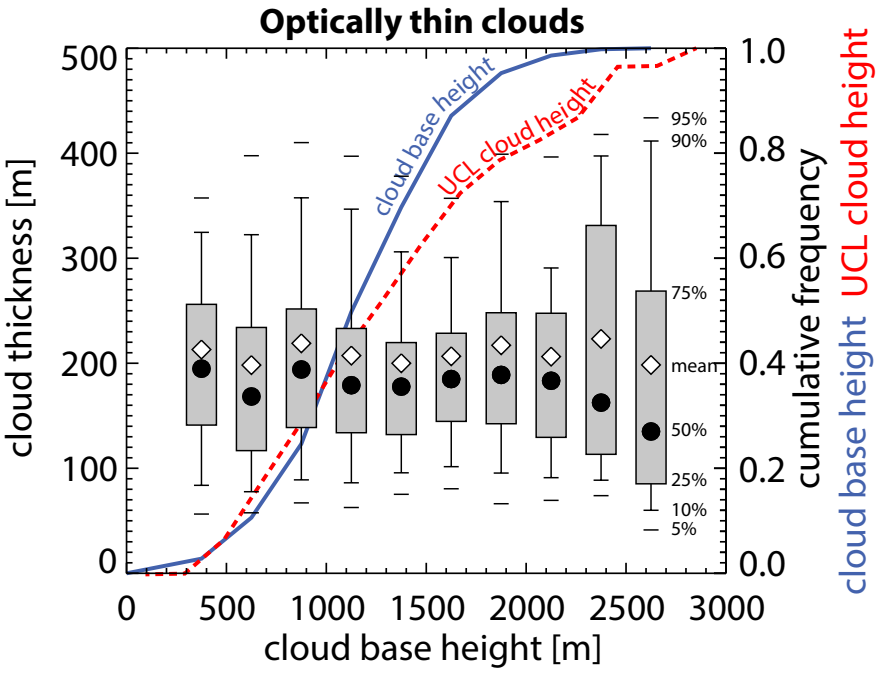

FIG. 13. Geometric thickness of optically thin low clouds sampled by the HSRL on the G-V aircraft during CSET, plotted against cloud base height (box-whiskers). Optically thin cloud layers are those that do not fully attenuate the HSRL beam, which is assessed using the HSRL signal to noise ratio. Here, we only include data from subcloud straight and level legs where the HSRL was nadir viewing. Box-whisker plots show percentiles of cloud thickness (5th ,10th, 25th, 75th, 90th, 95th percent) using box-whiskers, with black circles indicating medians and diamonds means. The solid blue line shows the cumulative frequency of cloud base height for optically thin clouds, indicating that the 10th and 90th percentiles of cloud base height for optically thin clouds are 625 m and 1700 m respectively, with a median of 1150 m. The red dashed line shows the cumulative frequency of the height at which *in situ* UCL cloud samples below 3 km altitude are found. It was not possible to determine the cloud base height of the UCL *in situ* cloud samples, but their low geometrical thickness suggests that the cloud base height associated with any given UCL *in situ* cloud sample would only be $\sim$100 m lower than the height of the sample on average. The 10th and 90th percentiles of UCL cloud height are 560 m and 2300 m respectively, with a median of 1250 m.